The GISS Model of the Global Atmosphere

R. C. J. SOMERVILLE, P. H. STONE, M. HALEM, J. E. HANSEN, J. S. HOGAN, L. M. DRUYAN, G. RUSSELL,[1] A. A. LACIS,[1] W. J. QUIRK AND J. TENENBAUM[2]

Institute for Space Studies, Goddard Space Flight Center, NASA, New York, N. Y. 10025

(Manuscript received 7 August 1973, in revised form 9 October 1973)

ABSTRACT

A model description and numerical results are presented for a global atmospheric circulation model developed at the Goddard Institute for Space Studies (GISS). The model version described is a 9-level primitive-equation model in sigma coordinates. It includes a realistic distribution of continents, oceans and topography. Detailed calculations of energy transfer by solar and terrestrial radiation make use of cloud and water vapor fields calculated by the model. The model hydrologic cycle includes two precipitation mechanisms: large-scale supersaturation and a parameterization of subgrid-scale cumulus convection.

Results are presented both from a comparison of the 13th to the 43rd days (January) of one integration with climatological statistics, and from five short-range forecasting experiments. In the extended integration, the near-equilibrium January-mean model atmosphere exhibits an energy cycle in good agreement with observational estimates, together with generally realistic zonal mean fields of winds, temperature, humidity, transports, diabatic heating, evaporation, precipitation, and cloud cover. In the five forecasting experiments, after 48 hr, the average rms error in temperature is 3.9K, and the average rms error in 500-mb height is 62 m. The model is successful in simulating the 2-day evolution of the major features of the observed sea level pressure and 500-mb height fields in a region surrounding North America.

1. Introduction

A multi-level numerical model of the global atmosphere has been developed recently at the Goddard Institute for Space Studies (GISS). This model has been used extensively for observing system simulation experiments, asynoptic data assimilation studies, and experimental long-range forecasting, largely in support of the Global Atmospheric Research Program (GARP) [e.g., Jastrow and Halem, 1973]. The model is based on the primitive equations of motion, solved by finite-difference methods in a global domain, as are other major general circulations models (e.g., Holloway and Manabe, 1971; Kasahara and Washington, 1971; Mintz, 1968; Arakawa, 1970). The resolution of the GISS model can be varied, but most development has been done with nine vertical levels and a horizontal grid spacing of 4° in latitude and 5° in longitude. Results obtained with this resolution are presented here.

The current form of the model may be thought of as the most recent generation of a continuing evolution of models at GISS. This evolution began with models developed at the University of California at Los Angeles (UCLA) by A. Arakawa and Y. Mintz, particularly their 3-level model (Arakawa, 1972). The GISS model shares the overall structure of this UCLA model and retains the σ-coordinate formulation of the equations, the Arakawa numerical method with advective quasi-conservation of important quadratic quantities, and much of the UCLA representation of physical processes occurring at and near the lower boundary of the atmosphere.

The GISS model differs from the UCLA model, however, not only in having finer vertical resolution, but also in its treatment of four crucial areas of physical processes: moist convection, turbulent subgrid-scale processes, solar radiation, and terrestrial radiation. In modeling these processes, many approximations and idealizations have necessarily been made. These have been influenced by considerations of computational economy, incomplete physical understanding, and intended model applications. The resulting parameterizations should be appropriate to a model which, like ours, is principally used for observing system simulations, asynoptic data assimilation studies, and experimental extended-range forecasting, rather than for long-term climate simulation. Indeed, we have been guided throughout the development of this model by the realization that these rather specialized uses would require a model somewhat different from either a conventional short-range numerical weather prediction model or a general circulation model. Thus, we have not been bound by the very high resolution and strin-

[1] Computer Sciences Corporation, New York, N. Y.
[2] State University of New York, Purchase, N. Y.

gent real-time requirements of the operational numerical forecaster, and we have simplified those aspects of the model which are important only on very long time scales. Similarly, we have chosen to verify our model both by short-range forecasts and by integrations which are intermediate in length between the few days of the operational forecast and the seasonal or annual or multi-annual period of climate simulation.

We have emphasized the development of treatments of the above physical processes since they are likely to be of crucial importance on time scales of a few weeks. In the next sections we describe these aspects of the model. Section 2 is a description of the model structure. The parameterization of moist convection is described in Section 3, and Section 4 outlines the treatment of surface characteristics and subgrid-scale diffusion. Sections 5 and 6 are concerned with the solar and terrestrial radiation calculations. In Section 7, the January climatology of the model is compared with that of the actual atmosphere. The results of five 2-day forecasts are presented in Section 8.

2. Model structure

The fundamental equations are the equation of motion, the equation of continuity, the equation of state, the first law of thermodynamics, the hydrostatic equation, and a conservation equation for water vapor. These equations, as summarized by Arakawa (1972), may be written, respectively, as follows:

$$\frac{d\mathbf{V}}{dt}+f\mathbf{k}\times\mathbf{V}+\nabla_\sigma\Phi+\sigma\alpha\nabla\pi=\mathbf{F} \tag{1}$$

$$\frac{\partial\pi}{\partial t}+\nabla_\sigma\cdot(\pi\mathbf{V})+\frac{\partial}{\partial\sigma}(\pi\dot{\sigma})=0 \tag{2}$$

$$p\alpha=RT \tag{3}$$

$$\frac{d\theta}{dt}=\frac{1}{c_p}\frac{\theta}{T}Q \tag{4}$$

$$\frac{1}{\pi}\frac{\partial\Phi}{\partial\sigma}=-\alpha \tag{5}$$

$$\frac{dq}{dt}=-C+E. \tag{6}$$

Here the notation is

$\mathbf{V}$	horizontal velocity
t	time
f	Coriolis parameter
$\mathbf{k}$	vertical unit vector
∇_σ	two-dimensional gradient operator
σ	the vertical coordinate $[=(p-p_t)/(p_s-p_t)]$
p	pressure
p_t	pressure at top of model atmosphere, constant
p_s	pressure at bottom of model atmosphere
α	specific volume
π	p_s-p_t
$\mathbf{F}$	horizontal frictional force
R	gas constant
T	temperature
θ	potential temperature
c_p	specific heat at constant pressure
Q	heating rate per unit mass
Φ	geopotential
q	water vapor mixing ratio
C	rate of condensation
E	rate of evaporation.

The frictional force $\mathbf{F}$ is described in Section 4. The heating rate Q includes contributions from large-scale condensation and subgrid-scale convection (Section 3), diffusion (Section 4), and radiation (Sections 5 and 6). The condensation rate C includes the moisture sink due to parameterized cumulus convection as well as the contribution from large-scale condensation (Section 3). Evaporation E occurs both at the lower boundary (Section 4) and in the interior of the atmosphere (Section 3).

A conventional dry convective adjustment is employed to stabilize super-dry-adiabatic lapse rates, but there is no "moist convective adjustment" (Manabe *et al.*, 1965). Instead, the GISS model incorporates the subgrid-scale moist convection parameterization described in Section 3.

The horizontal coordinates used are λ (longitude) and ϕ (latitude). In the version of the model which is presented here, the finite-difference mesh increments in the four independent coordinates are

$$\left.\begin{aligned}\Delta\lambda&=5^\circ\\ \Delta\phi&=4^\circ\\ \Delta\sigma&=1/9\\ \Delta t&=5\text{ min}\end{aligned}\right\}. \tag{7}$$

At the top of the atmosphere we choose $p_t=10$ mb, and at top and bottom we apply the boundary condition

$$\dot{\sigma}=\frac{d\sigma}{dt}=0 \quad \text{at} \quad \sigma=0,\ 1, \tag{8}$$

TABLE 1. Nominal pressures and approximate heights at the midpoints of the nine model layers.

Layer number	Nominal pressure at mid-layer (mb)	Approximate height at mid-layer (km)
1	65	20.2
2	175	13.0
3	285	9.7
4	395	7.4
5	505	5.5
6	615	4.0
7	725	2.7
8	835	1.6
9	945	0.6

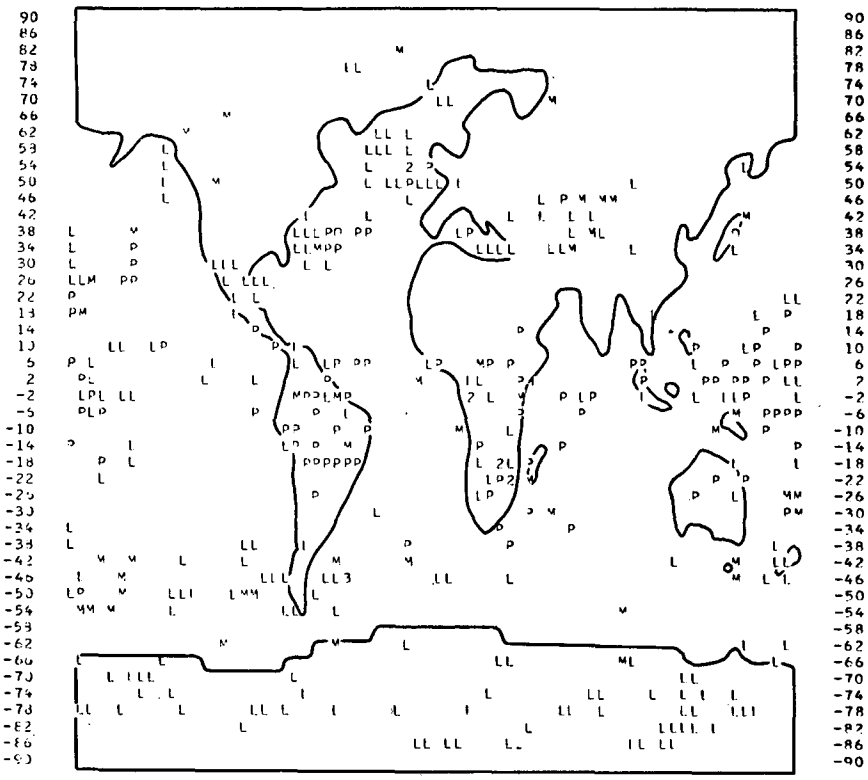

FIG. 1. Typical instantaneous array of computed convective clouds. Legend: L, low convection; M, middle convection; P, penetrating convection; 0, middle and penetrating convection; 2, low and penetrating convection; 3, low and middle and penetrating convection; blank, no convective clouds. Penetrating clouds prevail in the tropics, the summer hemisphere has more convective activity, and the continental influence is strong.

In Figs. 1–6, the ordinate is latitude, the abscissa is longitude with Greenwich at the center, and each character represents one horizontal grid point.

where σ is defined at the interfaces between the nine layers of the model atmosphere, while $\mathbf{V}$, T and q are defined at the midpoints of each layer. Other surface boundary conditions are described in Section 4. Approximate heights and pressures at the mid-points of the nine layers are given in Table 1.

The numerical method is due to Arakawa (1972). The distribution of variables over the horizontal grid points corresponds to his Scheme B, which is advantageous in simulating the geostrophic adjustment. The space differencing for the nonlinear advective terms in the equation of motion is constructed so as to maintain a constraint analogous (but not strictly equivalent) to mean square vorticity (enstrophy) conservation. In fact, the difference schemes for these terms reduce to the enstrophy- and kinetic-energy-conserving Jacobian scheme (Arakawa, 1966, 1970), when the mass flux is non-divergent. The resulting integral quasi-conservation of enstrophy as well as kinetic energy is an effective aid to preserving the shape of the energy spectrum as well as the area enclosed by it. The time-differencing scheme is a combination of the regular Matsuno and the time-alternating space-uncentered (TASU) Matsuno procedures (Arakawa, 1972; Chap. 8). In the present version of the GISS model, each simulated half-hour contains 10 min of TASU Matsuno steps and 20 min of regular Matsuno steps. To avoid reducing the time step in high latitudes, the zonal mass flux and zonal pressure force are smoothed longitudinally following the scheme described by Gates *et al.* (1971, Section IIID).

Integration of the above system, with the given resolution in the global domain, requires for each simulated day approximately 70 min of IBM 360/95 computer time. In the interests of computational economy, most aspects of the model representations of physical processes other than advection are calculated only every half-hour of simulated time. These processes include surface interaction and hydrology. Solar and terrestrial radiation calculations, however, are performed only every 2 hr of simulated time.

3. Moist convection

The GISS model contains two mechanisms for generating precipitation and cloudiness through condensation of water vapor. The first is large-scale supersaturation, which consists of a comparison at each

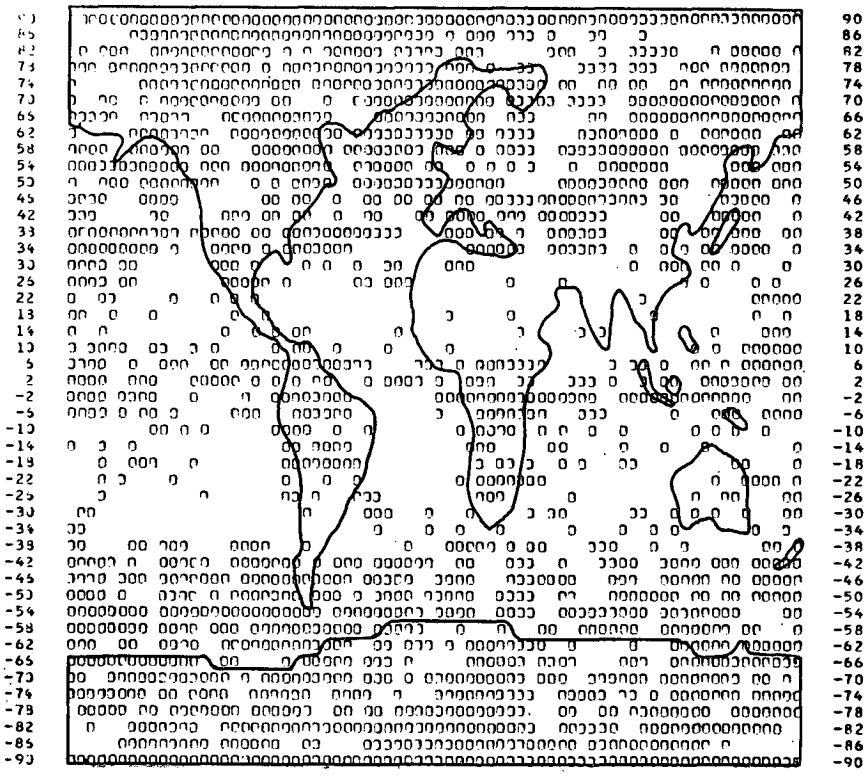

FIG. 2. Typical instantaneous array of computed total (convective plus supersaturation) clouds. A blank space indicates that no clouds are present, while a 0 is printed if any cloud is present in the column above the horizontal grid point.

grid point of the saturation and actual mixing ratios and, if necessary, an iterative reduction of the mixing ratio (accompanied by a rise in temperature due to latent heat release) until the relative humidity at the grid point equals 100%.

All condensation released by this process is assumed to evaporate in the next lower unsaturated layer or to precipitate if all lower layers are saturated. Each column of layers is tested from the top downward, and condensation in layer 9 precipitates. A cloud is assumed to be created at any grid point where condensation occurs. For purposes of radiative transfer calculations, properties of the cloud are assumed. For the terrestrial radiation calculation (Section 6), any cloud is assumed to be black in the infrared. For the solar radiation calculation, cloud properties depend on the cloud altitude and are determined on the basis of cloud climatology, as detailed in Section 5.

Small-scale moist convection, the second mechanism, is well-known to be crucial to the atmospheric budgets of heat, water and energy. It typically occurs on the space scale of cumulus clouds, 2–3 orders of magnitude smaller than the horizontal finite-difference mesh size. Thus, it cannot be resolved explicitly and must be treated parametrically. Such a parameterization may be regarded as an algorithm for uniquely determining the effect on the large-scale atmosphere of the small-scale convection, given the large-scale fields as calculated by the model. The assumption that such an algorithm exists is bold but necessary, since the cloud-scale fields cannot be neglected nor can they at present be calculated accurately.

The moist convection parameterization scheme in the GISS model is a generalization of Arakawa's scheme for the UCLA 3-level model (Arakawa *et al.*, 1969). At each horizontal grid point, the column of layers is examined every half-hour of simulated time as follows: pairs of layers are compared and convection occurs when a layer is buoyant in a certain sense with respect to a higher layer. Such convection stabilizes the column, and, like large-scale supersaturation, condenses water vapor, releases latent heat, and creates clouds for input to the radiation portion of the model. Model clouds are assumed to occupy the entire grid point area. Water vapor condensed in the moist convection parameterization is assumed to precipitate immediately.

For purposes of the pairwise comparison of layers, the 9 model layers may be treated individually or combined into fewer than 9 by "strapping" together two or more contiguous layers into thicker ones, whose properties are averages of the smaller layers which comprise them, and performing the comparison between the thicker "strapped" layers. Additionally, the

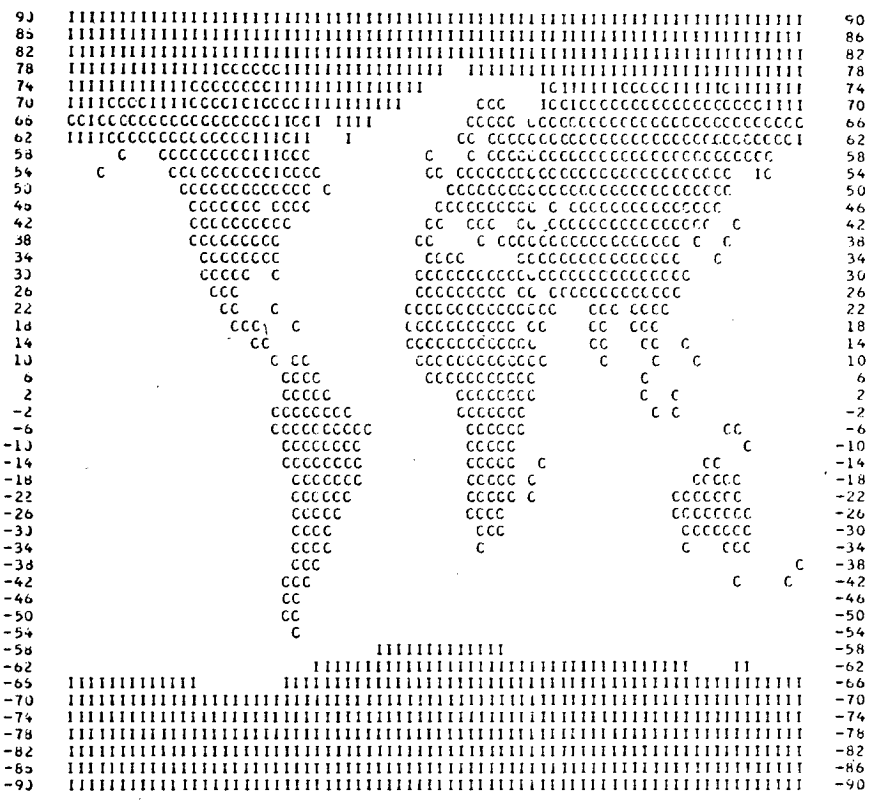

FIG. 3. Global distribution of land (C), ice (I) and sea (blank).

clouds formed when the convection criteria are satisfied may be assigned to one or more of the layers involved. Also, the radiative properties of the clouds, specified in Sections 5 and 6, introduce further degrees of freedom into the parameterization scheme.

In the current version of the GISS model, the three uppermost layers are ignored for purposes of moist convection, and the lower six layers are strapped into three, denoted by Roman numerals (I, II, III). Letting the 9 layers be numbered, as in Table 1, from 1 at the top to 9 at the bottom, we define layer I to be comprised of layers 8 and 9, layer II to be layers 6 and 7, and layer III to be layers 4 and 5. Then convection can occur between layers I and II (called low), between II and III (middle), and between I and III (penetrating).

The criteria for the three types of convection, as summarized by Haltiner (1971), are written in terms of the static energy H and saturation static energy H^*, defined by

$$H_n \equiv c_p T_n + g z_n + L q_n, \tag{9}$$

$$H_n^* \equiv c_p T_n + g z_n + L q_n^*, \tag{10}$$

where g is gravitational acceleration, z is altitude at mid-level, L the latent heat of vaporization, q the mixing ratio, q^* the saturation mixing ratio, and n, the level index, is I, II and III.

The criteria are

Low convection:	$H_{III}^* > H_I > H_{II}^*$
Middle convection:	$H_{II} > H_{III}^*$
Penetrating convection:	$H_I > (H_{III}^*, H_{II}^*) > H_{II}$.

It is clear that low and middle convection are interactions between pairs of adjacent layers, the lower being unstable with respect to the upper, while penetrating convection may be considered an instability between the lowest and highest layers. For the derivation of these criteria and the details of their implementation, see Arakawa (1972), Haltiner, and Arakawa *et al.* (1969).

The cloud assignment procedure, like the strapping, was arrived at through considerable numerical experimentation guided by cloud climatology. The following is current procedure:

Low convection: cloud is created at level 7 or 8, whichever has the larger relative humidity.

Middle convection: cloud is created at level 5 or 6, whichever has the larger relative humidity.

Penetrating convection: cloud is created in one of these sets of four contiguous layers: (4, 5, 6, 7), (5, 6, 7, 8), and (6, 7, 8, 9). A cyclic choice of set

FIG. 4. Global topography. Legend: 0, 0–250 m; 1, 250–500 m; 2, 500–750 m; 3, 750–1000m; 4, 1000–1500 m; 5, 1500–2000 m; 6, 2000–2500 m; 7, 2500–3000 m; 8, 3000–4000 m; 9, above 4000 m.

is made with the first and third sets each chosen 25% of the time and the second set chosen 50% of the time.

This cyclic feature may seem an unnecessary refinement, but we found that if deep clouds, which occur predominantly in the tropics, were assigned to only one altitude range, excessive longwave cooling occurred at the top of the resulting uniform cloud bank. The cyclic choice introduces a degree of heterogeneity to the model cloud population and enhances the realism of the radiative flux divergences.

The above parameterization produces a rather realistic cloud field, not only in terms of global average and latitudinal and longitudinal variation of percentage cloud cover, but also in that the tropical clouds are primarily convective, while middle and high latitudes are dominated by large-scale supersaturation clouds. Typical results for January are shown in Figs. 1 and 2.

4. Surface characteristics and subgrid-scale diffusion

In the GISS model the lower boundary may be land, sea, ice or snow. The locations of land, sea and ice are fixed and are shown in Fig. 3 for January. In higher latitudes, land locations may or may not be covered by snow, depending on the time of year. In the Northern Hemisphere, the latitude of the snow line in degrees is given by

$$\phi_s = 60 - 15\cos 2\pi\left(\frac{t-24.7}{365}\right), \tag{11}$$

where t is time measured in days, starting from 0000 GMT 1 January. The snow line in the Southern Hemisphere is always 120° south of this ϕ_s (Gates *et al.*, 1971). The albedos used in the model are 0.07 for sea, 0.14 for land, and 0.7 for ice and snow. Fig. 4 shows the elevation used for each surface grid point in the model, taken from Gates *et al.* Soil moistures, illustrated in Fig. 5, are based on the mean January values of Gates (1972).

The GISS model uses much the same treatment of boundary conditions and surface fluxes as does the UCLA model (Arakawa, 1972, Chap. 10). The surface stress and fluxes of sensible heat and water vapor are parameterized by drag laws, with the drag coefficients being functions of wind speed, static stability, type of surface, and surface height (to simulate mountain drag). An estimate of surface velocity is constructed by extrapolating the velocities in layers 8 and 9 to the lower boundary. An atmospheric surface temperature and

FIG. 5. Ground wetness (percent of saturation). Legend: 0, 0–5%; 1, 5–15%; 2, 15–25%; 3, 25–35%; 4, 35–45%; 5, 45–55%; 6, 55–65%; 7, 65–75%; 8, 75–85%; 9, 85–100%; S, snow on land; I, ice above sea level. Ice and snow are assumed to have 100% wetness.

specific humidity are defined by equating the fluxes of sensible heat and water vapor from the lower boundary to the same fluxes into layer 9. The change in boundary temperature for land, ice and snow locations is predicted from the net surface heating or cooling due to radiative, sensible heat, and latent heat fluxes. The details of these treatments are described by Arakawa (1972, Chap. 10). The boundary temperatures for sea locations are not calculated, but are specified, with the values depending on the calendar month. The values used are based on those of Washington and Thiel (1970). Fig. 6 illustrates the sea boundary temperatures used in January for the integration described in Section 7.

There is no explicit subgrid-scale horizontal diffusion in the model. Subgrid-scale vertical diffusion in layers 1–8 is parameterized by simple diffusion laws. The kinematic eddy viscosity, thermal diffusivity, and water vapor diffusivity in these layers are all fixed at 10^3 cm^2 sec^{-1} (Deardorff, 1967; Washington and Kasahara, 1970). Much larger values of the thermal diffusivity under statically unstable conditions are automatically simulated by the dry adiabatic adjustment and parameterized moist convective processes in the model. Simple diffusion laws are also used to parameterize the fluxes into layer 9 which are required to determine the atmospheric surface temperature and specific humidity discussed above. The thermal and water vapor diffusivities are given by formulas similar to those of Deardorff (1967) and Washington and Kasahara (1970). These diffusivities (cm^2 sec^{-1}) in layer 9 are given by

$$K=\begin{cases} 10^5+10^6\left[1-\exp\left(1.2\dfrac{\partial\theta}{\partial z}\right)\right], & \text{if } \partial\theta/\partial z\leqslant 0 \\ \dfrac{10^5}{1+40\ \mathrm{Ri}}+2\times 10^4, & \text{if } \partial\theta/\partial z>0 \end{cases}, \quad (12)$$

where $\partial\theta/\partial z$ is the static stability (°K km^{-1}) and Ri the local value of the Richardson number.

5. Absorption of solar radiation

A reliable calculation of the absorption of solar radiation is required in numerical circulation models for long-range weather forecasts as well as for climatological studies. In the computations of absorption it is important that the radiatively significant constituents of the atmosphere be treated as variables. This allows the circulation model to be used for investigating the effects of possible changes in the atmospheric composition, including "feedbacks" through the atmo-

FIG. 6. Sea surface temperature field for January. Legend: 0, 0–9C; 1, 9–10C; 2, 11–13C; 3, 13–15C; 4, 15–17C; 5, 17–19C; 6, 19–23C; 7, 23–25C; 8, 25–27C; 9, above 27C.

spheric dynamics which may magnify or diminish the initial effect of the changes.

In the GISS model the amount of solar energy absorbed at the earth's surface and in the atmosphere as a function of altitude is computed using a parametric method with the formulas and the coefficients based on accurate multiple-scattering computations. In this treatment the absorption varies with the amount and type of clouds, the humidity, the zenith angle of the sun, and the albedo of the earth's surface; within the stratosphere the absorption also depends on the ozone distribution. In the model, the solar zenith angle varies diurnally and seasonally, and the solar flux varies seasonally. The computing time requirements with this parametric method are small; the total computer time for the numerical circulation model is increased by only ~0.3% as compared to the case of no solar radiation calculations.

The parameterizations for each of the significant absorption and scattering processes are given in the following subsections. The accurate computations made outside of the circulation model and the methods for deducing the parameterizations are described in detail by Lacis and Hansen (1974).

a. Ozone absorption

Absorption of solar radiation by ozone contributes the major source of heating in the stratosphere (Manabe and Strickler, 1964), and should be incorporated in models which extend above ~15 km. Ozone absorption can be accurately parameterized, because most of it occurs where there is little scattering. Thus, the absorption is mainly of the direct solar beam and of diffuse radiation reflected upward by the lower atmosphere and ground.

If radiation with the spectral distribution of sunlight (Labs and Neckel, 1968) passes through an ozone amount x (cm, NTP) with no scattering, the fraction absorbed is

$$A_{oz}(x)=\frac{1.082x}{(1+138.6x)^{0.805}}+\frac{0.0658x}{1+(103.6x)^3}+\frac{0.02118x}{1+0.042x+0.000323x^2}, \quad (13)$$

with an error $\lesssim 0.5\%$ for 10^{-4} cm $\leqslant x \leqslant 1$ cm. The first two terms represent absorption in the ultraviolet and the third term absorption in the visual.

The ozone amount traversed by the direct solar beam in reaching the lth layer is

$$x_l=u_l M, \quad (14)$$

where u_l is the ozone amount in a vertical path above

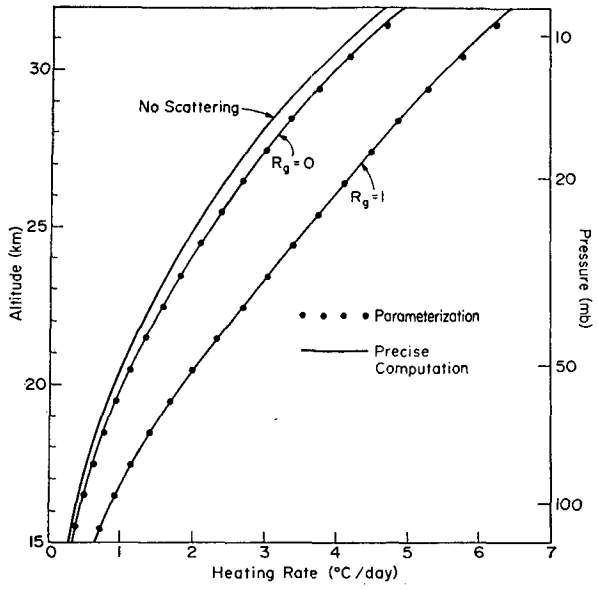

FIG. 7. Heating rates in the stratosphere due to ozone with the extreme ground albedos R_g of zero and unity. The two solid curves for different ground albedos were obtained with precise multiple-scattering computations and integrations over wavelength. The parameterizations were computed with (17). Also shown is the heating rate obtained if multiple scattering and ground reflection are neglected.

the lth layer,

$$M=\frac{35}{(1224\cos^2\theta_0+1)^{\frac{1}{2}}} \tag{15}$$

is a "magnification" factor (Rodgers, 1967) accounting for the slant path and refraction, and θ_0 is the local zenith angle of the sun. The ozone amount traversed by diffuse radiation illuminating the lth layer from below is

$$x_l^*=u_lM+1.9(u_t-u_l), \tag{16}$$

where u_t is the ozone amount in a vertical path above the effective reflecting layer (the ground for clear sky conditions, or the cloud top for cloudy skies); the factor 1.9 is an average magnification factor for the diffuse upward radiation.

Thus, the parametric formula for ozone absorption in the lth layer of the atmosphere is

$$A_{l,oz}=S_0\cos\theta_0\{A_{oz}(x_{l+1})-A_{oz}(x_l)+R[A_{oz}(x_l^*)-A_{oz}(x_{l+1}^*)]\}, \tag{17}$$

where S_0 is the solar flux and R the albedo of the lower atmosphere and ground, obtained as follows. If no clouds are present, the albedo of the atmosphere is taken to be the effective albedo due to Rayleigh scattering (averaged over the ozone bands):

$$\bar{R}_a(\theta_0)=\frac{0.219}{1+0.816\cos\theta_0}. \tag{18}$$

In the case of cloudy skies, $\bar{R}_a$ is taken to be the cloud albedo. In either case, the albedo of the atmosphere is combined with that of the ground to obtain

$$R=\bar{R}_a(\theta_0)+[1-\bar{R}_a(\theta_0)](1-\bar{\bar{R}}_a)R_g/(1-\bar{\bar{R}}_aR_g), \tag{19}$$

where $\bar{\bar{R}}_a$ is the average of $\bar{R}_a(\theta_0)$ for all solar angles, and the denominator in the last term accounts for multiple reflections between atmosphere and ground.

Fig. 7 compares heating rates computed from (17) with the results of precise multiple-scattering computations. These are instantaneous heating rates for a solar zenith angle of 40°. For this illustration Green's (1964) formula was used for the vertical ozone distribution, with 0.4 cm of ozone and the altitude of the ozone maximum at 20 km. The precise computations were made using ~200 wavelengths and the vertical distribution of Rayleigh scatterers given by the U. S. Standard Atmosphere (Champion *et al.*, 1962). Also shown in Fig. 7 is the heating rate which would be obtained if multiple scattering and ground reflection were neglected.

b. Water vapor absorption

The solar heating of the troposphere is primarily due to absorption by water vapor, which has a highly frequency-dependent absorption coefficient. Solution of the transfer equation and integration over frequency are impractical, but a parameterization can be devised from laboratory transmission functions.

The absorption by the major water vapor bands has been measured at low spectral resolution by Howard *et al.* (1956). These absorbtivities have been weighted with the solar flux and summed over all of the measured bands by Yamamoto (1962) to obtain the total absorption as a function of water vapor amount y (centimeters of precipitable water vapor). The formula

$$A_{wv}(y)=\frac{2.9y}{(1+141.5y)^{0.635}+5.925y} \tag{20}$$

fits Yamamoto's absorption curve with an error $\lesssim 1\%$ for 10^{-2} cm $\leqslant y \leqslant 10$ cm. Eq. (20) applies for pressure $p_0=1013$ mb and temperature $T_0=273$C, but the pressure and temperature dependence of the absorption are approximately accounted for by using an effective water vapor amount

$$y^{\text{eff}}=y\frac{p}{p_0}\left(\frac{T_0}{T}\right)^{\frac{1}{2}}. \tag{21}$$

In the spectral regions of significant water vapor absorption Rayleigh scattering is negligible. Thus, for *clear skies* the absorption by water vapor in the lth layer can be obtained immediately as

$$A_{l,wv}=S_0\cos\theta_0\{A_{wv}(y_{l+1})-A_{wv}(y_l)+R_g[A_{wv}(y_l^*)-A_{wv}(y_{l+1}^*)]\}, \tag{22}$$

TABLE 2. Discrete probability distribution of water vapor absorption coefficients for $N=6$.

n	k_n	$P(k_n)$
1	7×10^{-5}	0.647
2	0.005	0.107
3	0.041	0.104
4	0.416	0.073
5	4.75	0.044
6	72.5	0.025

where y_l is the effective water vapor amount traversed by the direct solar beam in reaching the lth layer, R_g is the ground albedo, and y_l^* is the effective water vapor amount in the upward path between the ground and layer l (including an average magnification factor 5/3).

For *cloudy skies* the absorption formula is no longer applicable. In this case the absorption is obtained from approximate multiple-scattering computations in conjunction with a probability distribution for the absorption coefficient k. A distribution function $P(k)$ is extracted from the laboratory transmissivities,

$$T_{wv}(y)=1-A_{wv}(y)=\int_0^\infty P(k)e^{-ky}dk, \qquad (23)$$

by replacing the integral in (23) with a sum over k_n, $n=1$, N, and numerically inverting the equation to obtain N values for $P(k_n)$. Table 2 gives values of k_n and $P(k_n)$ for $N=6$ which fit the transmission in (23) within 0.1% for 10^{-2} cm$\leqslant y\leqslant$ 10 cm.

The cloud optical thickness τ is assigned according to the cloud type, as indicated in Table 3. For example, with the 9-layer GISS model, middle-level convection can put a cloud in either layer 5 or layer 6 with an optical thickness of 8. Penetrating convection puts a cloud in four consecutive layers, each with an optical thickness of 8. Large-scale supersaturation can put clouds in any number of layers, with the optical thickness being 0, 1, 2, 4, 6, 6, 8, 8 and 8 for the nine layers, respectively. For example, if there are clouds due to large-scale supersaturation in the lowest three layers, the total optical thickness may be 8, 16 or 24, depending on the number of layers occupied; this allows a variation of cloud optical properties about the climatological average.

TABLE 3. Visual albedo and optical thickness as a function of cloud type.

Cloud origin		Assumed cloud type	Visual albedo	Optical thickness
Small-scale moist convection	middle-level	Ac	~50%	~8
	low-level	Cu	~70%	~16
	penetrating	Cb	~80%	~32
Large-scale supersaturation	0–400 mb	Ci	~20%	~2
	400–700 mb	As	~50%	~8
	700–1000 mb	St	~70%	~16

From the optical thickness and specific humidity, the single-scattering albedo for each layer of the atmosphere and each value of k_n is obtained:

$$\tilde{\omega}_{l,n}=\frac{\tau_l}{\tau_l+k_n w_l}, \qquad (24)$$

where w_l is the effective water vapor amount in a vertical path within the lth layer; this represents a crude correction for the effects of atmospheric inhomogeneity. From $\tilde{\omega}_{l,n}$, τ_l, θ_0 and R_g the absorption in each layer is computed with the following scheme [for details and equations see Lacis and Hansen (1974)]:

1) For each layer of the atmosphere and each k_n, the reflection, absorption and transmission are approximated with analytic functions which depend on $\tilde{\omega}$ and τ.

2) The layers are combined to obtain the flux distribution of solar radiation throughout the atmosphere; the procedure is based on the "adding" method, but it is assumed that the diffuse transmission through a cloud is isotropic so that no integrations over angle are involved.

3) The total absorption in each layer is obtained by summing over the $N-1$ (=5) values of k_n which are significant.

Fig. 8 shows a typical example of computed heating rates in the troposphere for clear sky conditions and for two different cloud types. The major effect of the clouds is to increase the heating rate within the clouds and decrease it beneath the clouds. The increased heating within the clouds is due to the increased photon path due to multiple scattering. The decreased heating

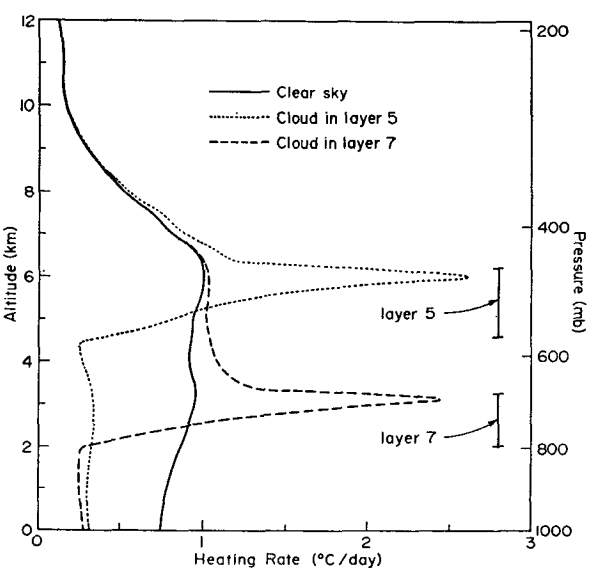

FIG. 8. Heating rates in the troposphere due to solar radiation. The curves illustrated are typical results with a clear sky and with clouds in a single layer. Each of the clouds in this example has an optical thickness of 8.

in lower layers is a consequence of the reduced solar flux beneath the clouds.

c. Surface absorption

Solar radiation transmitted by the atmosphere is subject to possible absorption by the earth's surface. The amount of absorption is computed as the sum of two terms, one ($A_{g,1}$) for the wavelength region where the absorption coefficient of water is significant and one ($A_{g,2}$) for the remaining wavelengths. Approximately 35% of the solar flux is contained in the regions of significant water vapor absorption, as indicated by the probability distribution $P(k)$ of Table 2; the same percentage is obtained from the assumption that water vapor absorption is significant only for wavelengths> 0.9 μm (Joseph, 1971).

For clear skies, $A_{g,1}$ follows from the results of the previous section:

$$A_{g,1}=S_0\cos\theta_0[0.353-A_{wv}(Mw_t)](1-R_g), \quad (25)$$

where w_t is the effective water vapor amount in a vertical column above the ground. For cloudy skies, $A_{g,1}$ is obtained by multiplying the total downward flux at the ground for each value of k_n by $(1-R_g)$ and summing over n from 2 to N.

For the spectral region of negligible water vapor absorption the effect of Rayleigh scattering is significant and is included in the computations of absorption by the surface. For clear skies

$$A_{g,2}=S_0\cos\theta_0[0.647-\bar{R}_r(\theta_0)-A_{oz}(Mu_t)]\times(1-R_g)/(1-\bar{R}_r^*R_g), \quad (26)$$

where u_t is the ozone amount in a vertical path above the ground, $\bar{R}_r(\theta_0)$ is the albedo of the Rayleigh atmosphere for the total solar spectrum, given within $\sim$1% by

$$\bar{R}_r(\theta_0)=\frac{0.28}{1+6.43\cos\theta_0}, \quad (27)$$

and $\bar{R}_r^*=0.0685$ is the spherical albedo of the Rayleigh atmosphere for illumination from below. For cloudy skies

$$A_{g,2}=S_0\cos\theta_0[0.647-A_{oz}(Mu_t)]\times(1-R_c)(1-R_g)/(1-R_cR_g), \quad (28)$$

where u_t is the ozone amount in a vertical path above the highest cloud layer and R_c the total cloud albedo.

d. Numerical parameters

In the model computations for which numerical results are reported in this paper, the ground albedo followed the simple scheme: 0.07 for oceans, 0.14 for land, and 0.70 for snow or ice. The total ozone amount in a vertical column varied with season and latitude according to Fig. 10 of Manabe and Möller (1961), the range being $\sim$0.23 cm to $\sim$0.43 cm. The vertical distribution of ozone was assumed to be a function of the total ozone amount, with numerical values obtained from Fig. 11 of Manabe and Möller.

6. Terrestrial radiation

The method for treating terrestrial (longwave) radiation involves a non-grey treatment of radiative transfer, with an adjustable degree of greyness. The surface temperature, atmospheric temperature and humidity profiles, and clouds generated elsewhere in the dynamical model are used to calculate the longwave heating or cooling rates in the 9 layers.

Accurate determination of the longwave heating or cooling requires an accurate calculation of the optical thickness of the atmosphere above each of the boundaries of the model layers. In the present treatment, available information on the positions, intensities and half-widths of water vapor and carbon dioxide lines, as well as laboratory data on the absorption of water vapor, are utilized to accurately simulate the absorptive properties of the atmosphere.

The highest spectral resolution obtainable with this scheme is 53 spectral intervals between 4 μm and ∞. This mode consists of 50 absorbing intervals of uniform width (20 cm^{-1}) between 10 μm and ∞, one absorbing interval between 4.9 and 8.7 μm, and two window regions, 4.0–4.9 μm and 8.7–10 μm, where the atmospheric opacity is assumed to be zero. Opacity in the 9.6-μm ozone band is neglected because it has a minor effect on tropospheric heating rates. The degree of greyness between 10 μm and ∞ can be varied by Planck-mean averaging of the opacity in the 50 basic intervals into 25, 10, 5, 2 or 1 interval as desired. The results described below were achieved using five spectral intervals between 10 μm and ∞. The intervals, in microns, were 10 to 12.5, 12.5 to 16.6, 16.6 to 25, 25 to 50, and 50 to ∞.

The rotation band of H_2O is a major source of atmospheric opacity between 10 μm and ∞. The opacity due to this band in each of the 50 basic spectral intervals is calculated by means of a random-exponential band model, which assumes an ideal array of randomly spaced lines of Lorentzian shape, with an exponential distribution of line intensities. This model should accurately simulate the actual absorption in the atmosphere due to the H_2O rotation band.

For the random-exponential band model, optical thickness in a spectral interval $\Delta\nu$ can be expressed as

$$\tau=2\pi yu(2u+1)^{-\frac{1}{2}}, \quad (29)$$

where y and u can be regarded as dimensionless pressure and path length, respectively. In terms of the intensity $S(j,T)$ and Lorentz half-width $\alpha(j,T)$ of the jth spectral line, y and u are given, at temperature

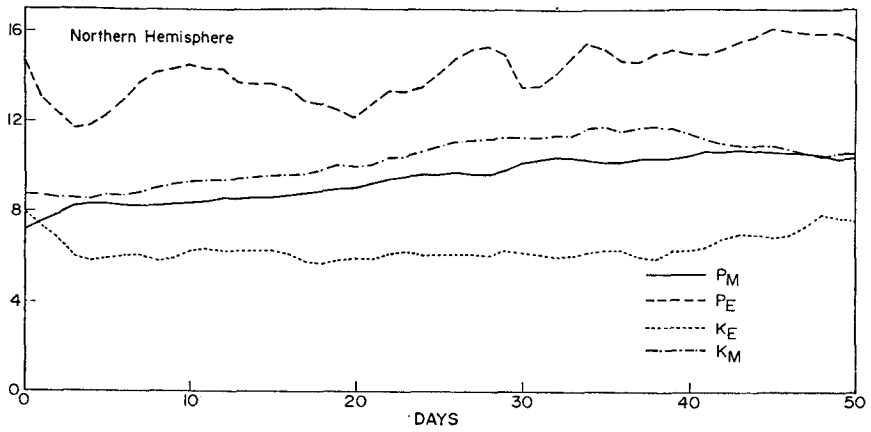

FIG. 9. Time evolution, in the Northern Hemisphere model troposphere (layers 2–9) of the integrated zonal available potential energy (P_M), eddy available potential energy (P_E), eddy kinetic energy (K_E), and zonal kinetic energy (K_M). Units: P_M, 10^6 J m^{-2}; P_E, K_E, K_M, 10^5 J m^{-2}.

T, by

$$y(T)=\frac{4p}{\pi\Delta\nu}\{\sum_{j=1}^{N}[S(j,T)\alpha_0(j,T)]^{\frac{1}{2}}\}^2/\sum_{j=1}^{N}S(j,T), \quad (30)$$

$$u(T)=\frac{a}{8p}\{\sum_{j=1}^{N}S(j,T)/\sum_{j=1}^{N}[S(j,T)\alpha_0(j,T)]^{\frac{1}{2}}\}^2, \quad (31)$$

where a is the absorber amount, p the pressure in fractional atmospheres, N the number of spectral lines in the wavenumber interval $\Delta\nu$, and $\alpha_0(j,T)$ the Lorentz half-width of the jth line at a pressure of 1 atm and temperature T.

The parameters

$$\sum_{j=1}^{N}S(j,T)\ [\text{gm}^{-1}\ \text{cm}]$$

$$\sum_{j=1}^{N}[S(j,T)\alpha_0(j,T)]^{\frac{1}{2}}\ [\text{gm}^{-\frac{1}{2}}]$$

were tabulated in external calculations at temperatures of 200, 250 and 300K from the H_2O line data of Benedict and Kaplan (1959) and unpublished data of Benedict. A linear interpolation (or extrapolation) is performed at each grid point to obtain the values of these parameters appropriate to the model temperature profile, i.e., corresponding to the mean (H_2O weighted) temperature of the model layers above the level at which the optical thickness is to be evaluated. The absorber amount a is taken to be the total H_2O amount (gm cm^{-2}) above this level and the characteristic pressure p is taken to be the mean (H_2O weighted) pressure above this level.

The CO_2 vibration-rotation band near 15 μm greatly increases the atmospheric opacity between 11.6 and 20 μm. CO_2 optical thicknesses in this region were calculated externally for a standard atmosphere from line data of Drayson and Young (1967), taking into account absorption by 2219 CO_2 lines, and assuming a constant CO_2 mixing ratio of 3.3×10^{-4} by volume. Detailed line-by-line integration of CO_2 absorption coefficients was

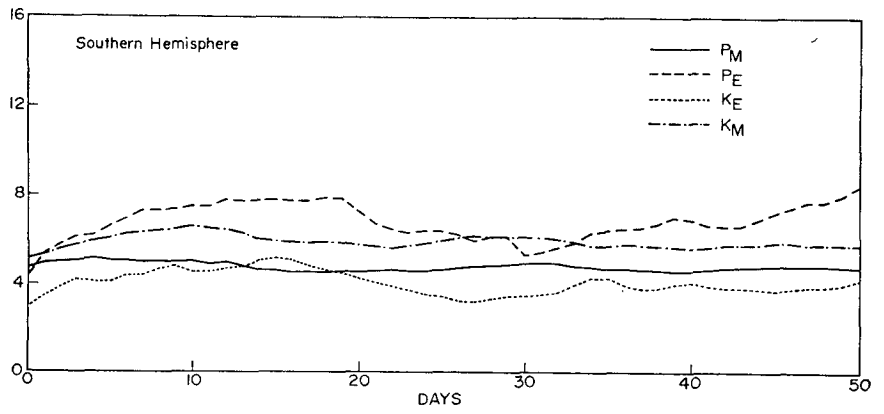

FIG. 10. As in Fig. 9 except for the Southern Hemisphere.

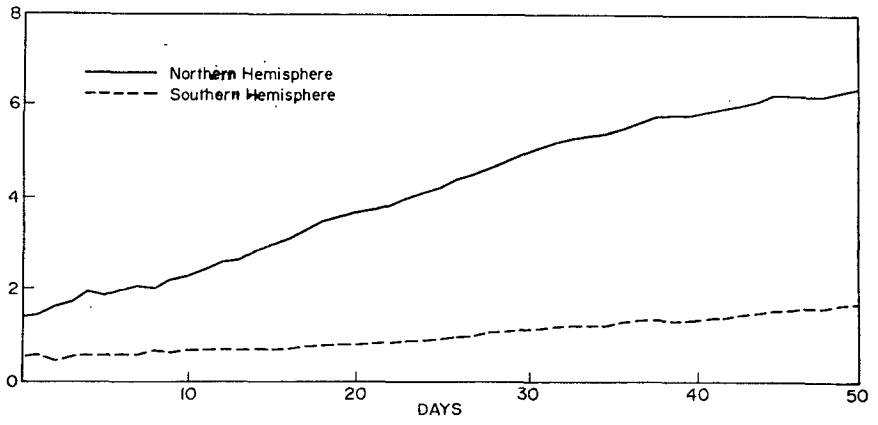

FIG. 11. Time evolution of zonal kinetic energy (10^5 J m^{-2}) in the two hemispheres of the model stratosphere (layer 1).

performed, assuming a Lorentz line shape, with a half-width of 0.08 cm^{-1} at a pressure of 1 atm and a temperature of 273K.

The optical thickness at wavenumber ν for a temperature T and pressure p is given by

$$\tau(\nu)=\frac{b\alpha(T,p)}{\pi}\sum_{j=1}^{2219}\frac{S(j,T)}{(\nu-\nu_j)^2+\alpha(T,p)^2}, \qquad (32)$$

where b is the amount of CO_2 (gm cm^{-2}) above the level under consideration, $\alpha(T,p)$ the Lorentz half-width (cm^{-1}), taken to be the same for all CO_2 lines, and ν_j the central wavenumber of the jth line. Monochromatic opacities for the standard atmosphere were calculated at a spacing of 0.001 cm^{-1} in the spectral region between 11.6 and 20 μm. These monochromatic opacities were then averaged, to obtain the mean opacities due to the 15-μm CO_2 band, over the spectral intervals used in the model calculations.

From independent numerical experiments, it was found that a linear representation of the dependence of the CO_2 opacity on effective pressure reduced the accuracy of the net flux determinations by 5–10% relative to a more detailed treatment, taking the exact pressure and temperature dependence into account. In the interests of economy of computer time, such a representation was adopted in the calculations described

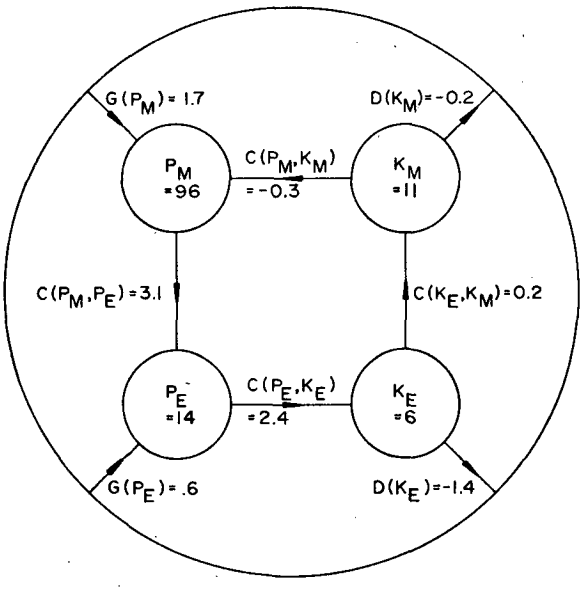

FIG. 12a. Northern Hemisphere energy cycle in the space domain for the GISS model (levels 2–9) January mean. Units: energy, 10^5 J m^{-2}; conversions, W m^{-2}. The conversions are generation (G), dissipation (D), and internal conversion $C(a,b)$. $C(a,b)$ is positive if energy flows from a to b. The forms of energy are zonal available potential energy (P_M), eddy available potential energy (P_E), eddy kinetic energy (K_E), and zonal kinetic energy (K_M). For detailed definitions, see Oort (1964).

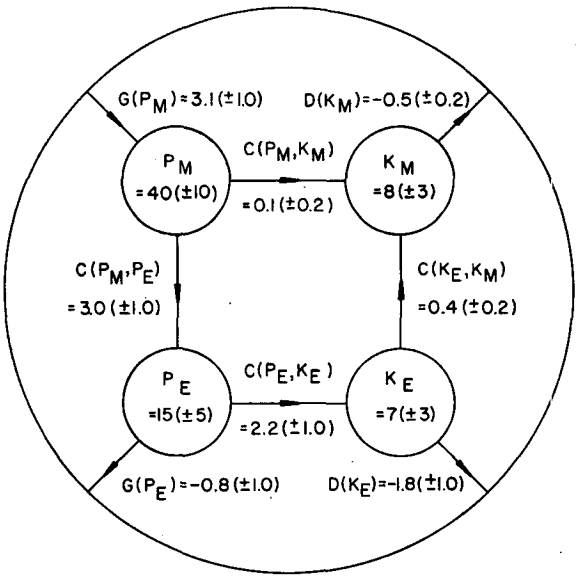

FIG. 12b. As in Fig. 12a except for observed atmospheric annual mean compiled by Oort (1964).

here. The optical thickness of CO_2 obtained in this manner was then added, at each level, to the optical thickness of H_2O derived as outlined above.

The H_2O vibration-rotation (6.3 μm) band is mainly responsible for the atmospheric opacity between 4.9 and 8.7 μm. In the present treatment, this opacity is calculated from empirical formulas derived from low-resolution laboratory measurements of Howard *et al.* (1956). Two formulas are used for the total band area A between 2050 cm^{-1} (4.88 μm) and 1150 cm^{-1} (8.7 μm):

$$A=3.56\times10^{2}a^{0.5}p^{0.3}, \quad \text{for} \quad A>160 \text{ cm}^{-1}, \tag{33}$$

$$A=3.02\times10^{2}+2.18\times10^{2}\log_{10}a+1.57\times10^{2}\log_{10}p, \quad \text{for} \quad A<160 \text{ cm}^{-1}, \tag{34}$$

where p is the characteristic pressure (mm Hg), and a the H_2O amount (gm cm^{-2}). The average optical thickness in the interval from 1150 to 2050 cm^{-1} is thus

$$\tau=-\ln\left(1-\frac{A}{900}\right). \tag{35}$$

In the model calculations, the optical thickness is evaluated using the mean (H_2O weighted) pressure above a given level and the total H_2O amount above this level, with the constraint that A not be allowed to exceed 900 cm^{-1}. In situations where $A>900$ cm^{-1}, the optical thickness is computed by extrapolating downward from the lowest level at which $A<900$ cm^{-1}, assuming the opacity to increase linearly with a.

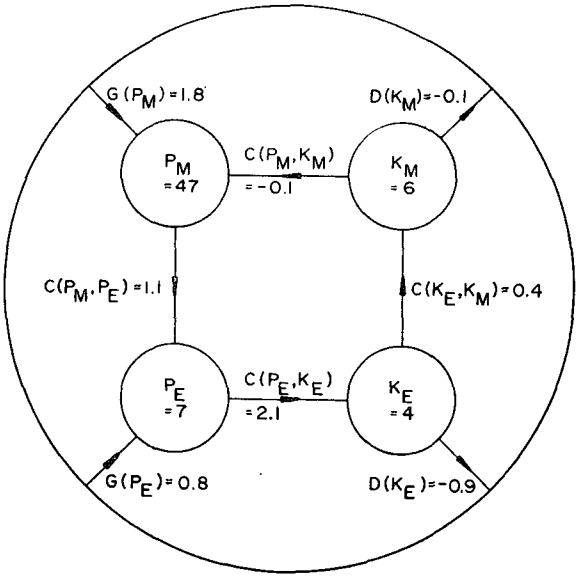

FIG. 13. Southern Hemisphere energy cycle for the GISS model (levels 2–9) January mean. Definitions as in Fig. 12a.

To obtain more precise estimates of the longwave radiative fluxes, the number of layers in the dynamical model is doubled for purposes of the radiative transfer calculation. Average temperatures and humidities in the refined layers are obtained by interpolation of the model-generated temperatures and humidities. If clouds

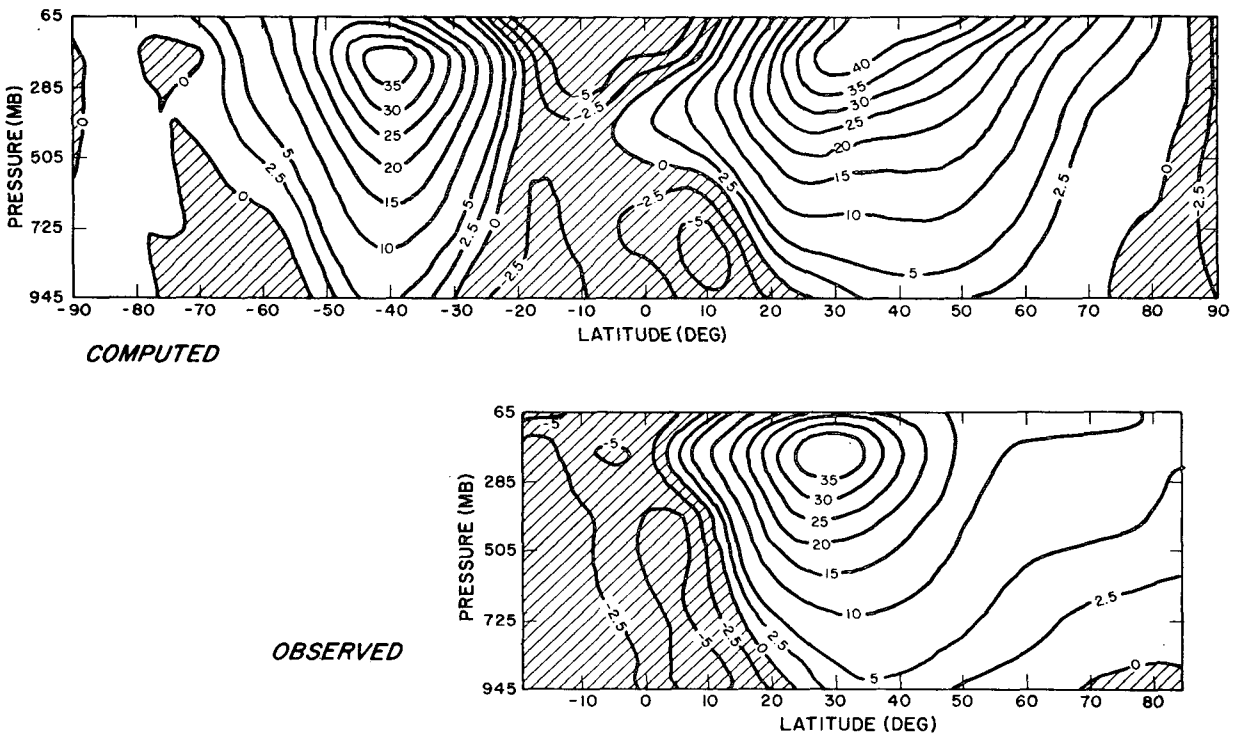

FIG. 14. Computed and observed January zonal mean fields of zonal wind (m sec^{-1}). Observed field is based on data from Oort and Rasmusson (1971). Negative (easterly) regions are shaded.

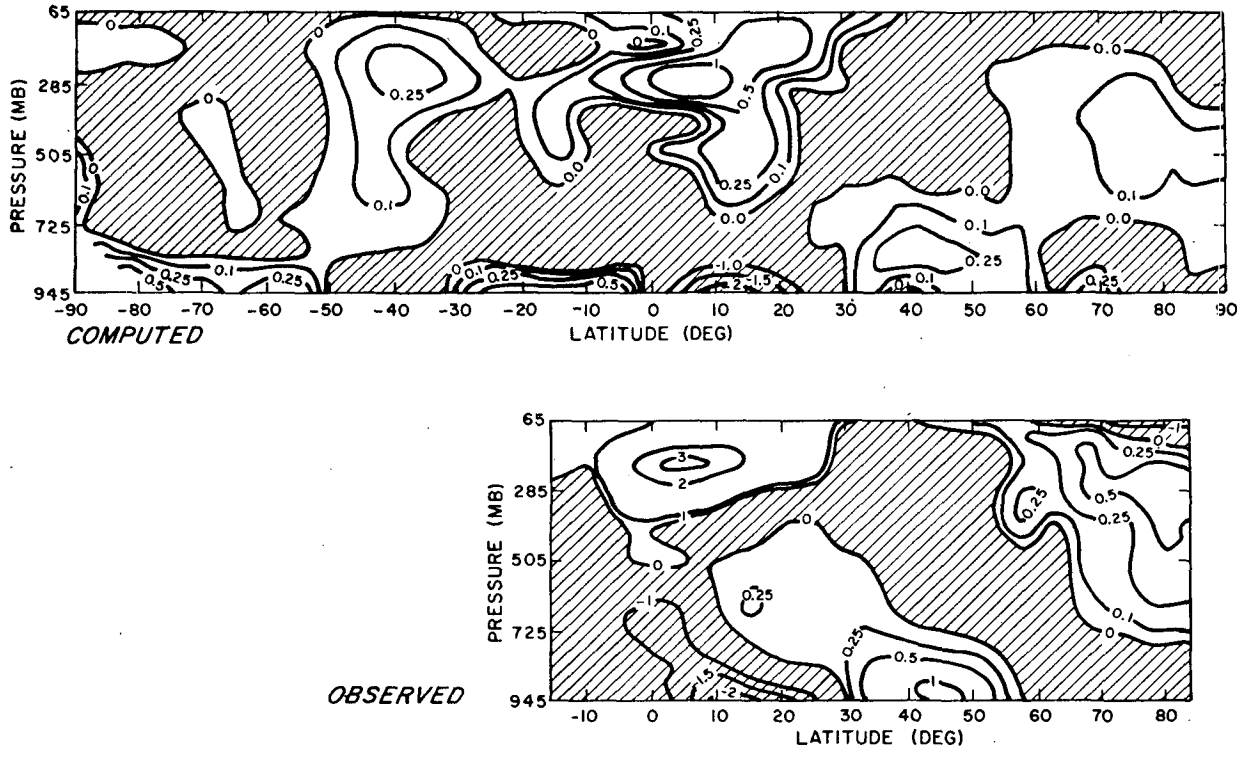

FIG. 15. Computed and observed January zonal mean fields of meridional wind (m sec^{-1}). Observed field is based on data from Oort and Rasmusson (1971). Negative (southward) regions are shaded.

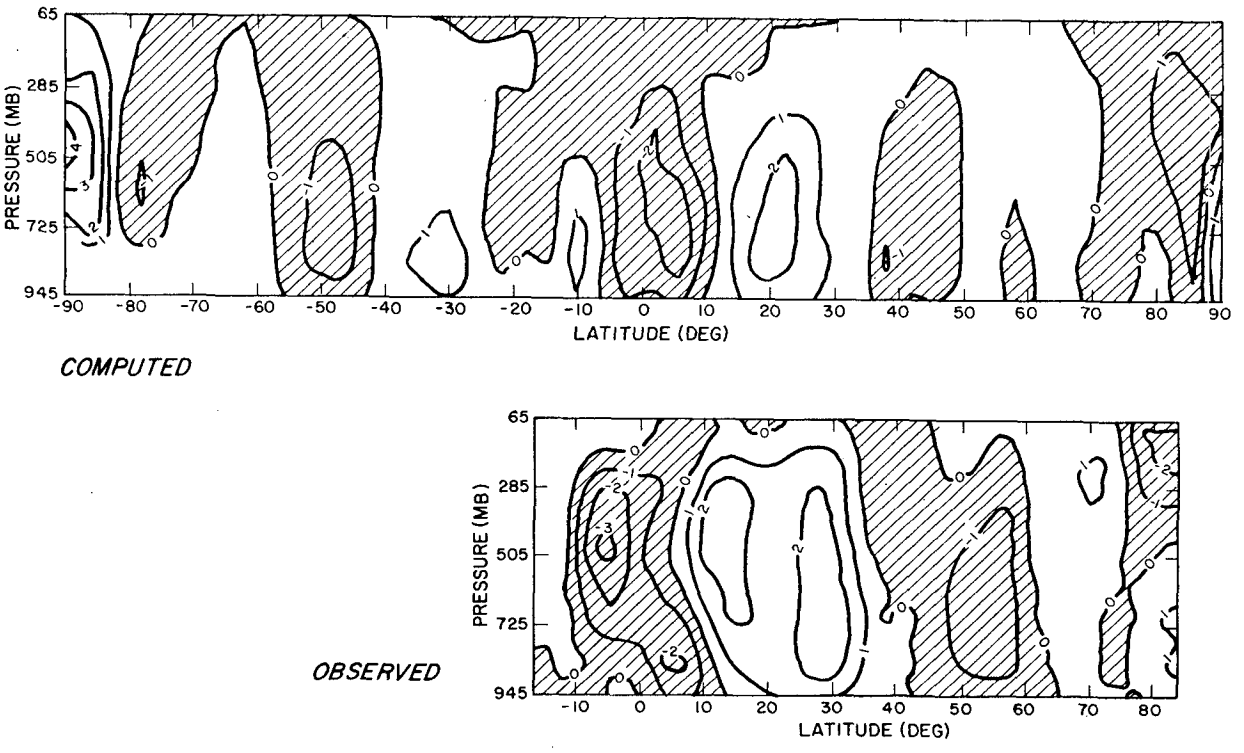

FIG. 16. Computed and observed January zonal mean fields of vertical wind (omega, 10^{-4} mb sec^{-1}). Observed field is based on data from Oort and Rasmusson (1971). Negative (upward) regions are shaded.

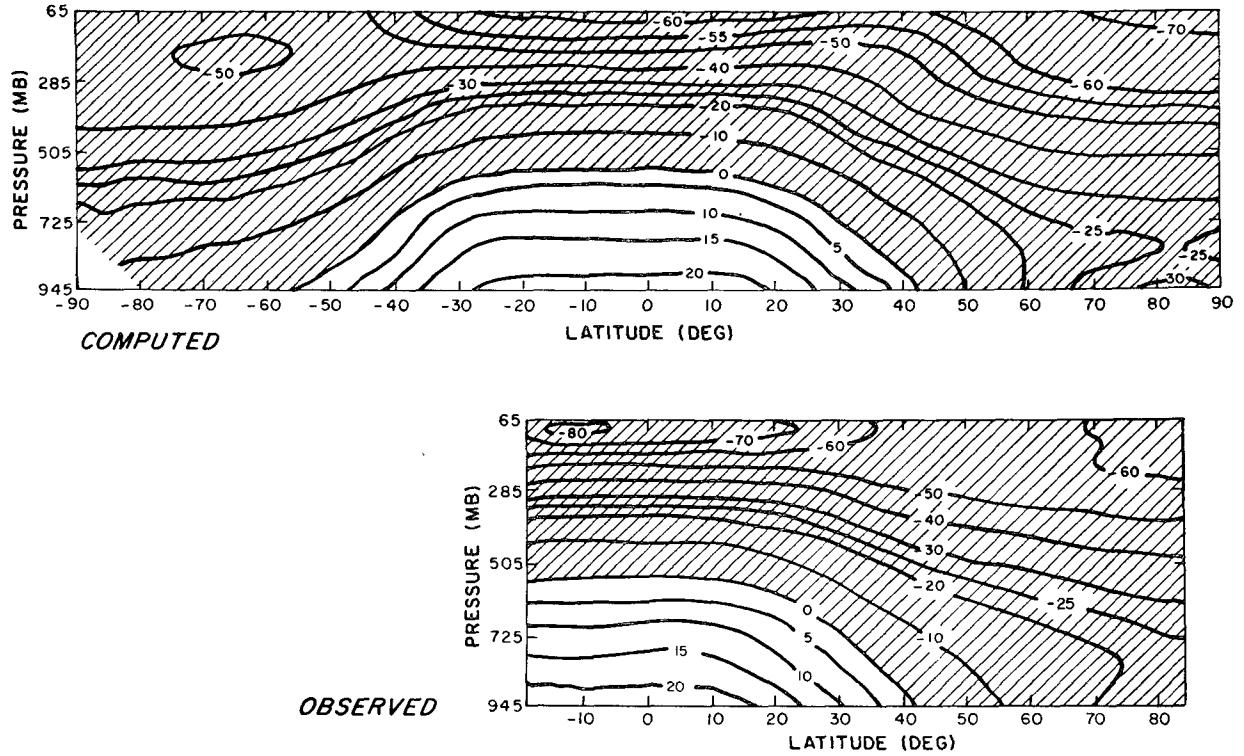

FIG. 17. Computed and observed January zonal mean fields of temperature (°C). Observed field is based on data from Oort and Rasmusson (1971). Negative regions are shaded.

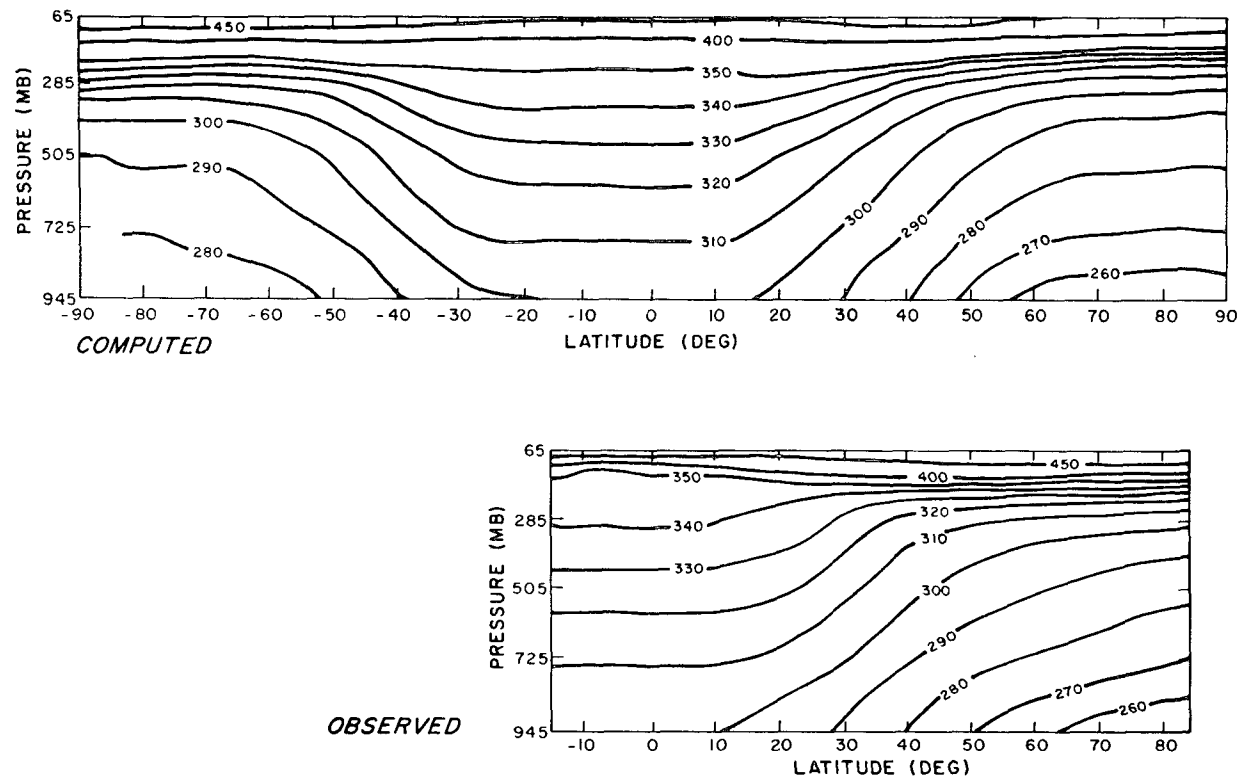

FIG. 18. Computed and observed January zonal mean field of potential temperature (°K). Observed field is based on data from Oort and Rasmusson (1971).

are present in a layer of the dynamical model, they are assumed to fill the two corresponding layers in the longwave radiative transfer calculation. Also, to properly simulate the longwave fluxes at the upper boundary of the dynamical model, two additional layers are added between 1 and 10 mb. The mean temperatures in these layers are derived from climatological data provided by R. Newell (private communication) by interpolation in space and time. Relative humidity in these layers is obtained by extrapolating upward, assuming that the relative humidity decreases from the value given for the top layer of the dynamical model, in proportion to the pressure.

The tops and bottoms of clouds as well as the earth's surface serve as boundaries in the longwave flux calculations. When clouds exist in a layer, they are assumed to occupy the full vertical extent of that layer. Clouds and ground are treated as perfect absorbers and emitters of longwave radiation (blackbodies). The net flux F at a level between two cloudy layers i and $i+1$ is obtained by subtracting the downward blackbody flux (integrated over all wavelengths) from the upper layer (i) from the upward black body flux from the lower layer ($i+1$):

$$F=\sigma(T_{i+1}^4-T_i^4). \tag{36}$$

The net flux at the ground, F_g, when there is a cloud in the lowest (jth) refined layer, adjacent to the ground, and the ground temperature is T_g, is calculated from

$$F_g=\sigma(T_g^4-T_j^4). \tag{37}$$

At other levels, four longwave fluxes are calculated from the standard equations of radiative transfer:

1) F_1—direct flux from the bottom of the nearest cloud at higher levels, if any is present:

$$F_1=2\pi\int_0^{2500\text{ cm}^{-1}} B_\nu(T_c)\,\mathrm{Ei}_3[\tau_0(\nu)-\tau_c(\nu)]d\nu, \tag{38}$$

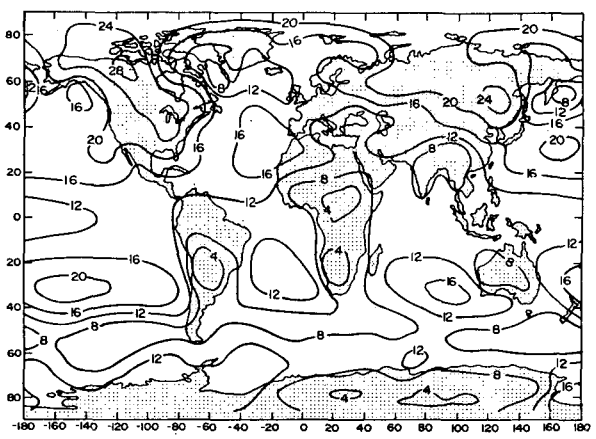

FIG. 19. Computed January mean sea level pressure field. Units: millibars −1000.

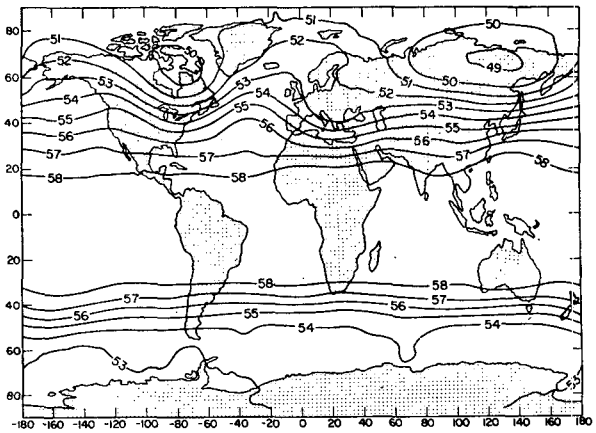

FIG. 20. Computed January mean 500-mb height field (10^2 m).

where subscript c refers to the cloud and 0 to the boundary between layers i and $i+1$.

2) F_2—direct flux from the nearest cloud at lower levels, if any is present:

$$F_2=2\pi\int_0^{2500\text{ cm}^{-1}} B_\nu(T_c)\,\mathrm{Ei}_3[\tau_c(\nu)-\tau_0(\nu)]d\nu. \tag{39}$$

If no cloud is present, T_c and τ_c are replaced by T_g and τ_g, the optical depth of the ground.

3) F_3—flux originating in the clear atmosphere higher up:

$$F_3=2\pi\int_0^{2500\text{ cm}^{-1}}\int_{0\text{ or }\tau_c}^{\tau_0} B_\nu[T(t)]\times\mathrm{Ei}_2[\tau_0(\nu)-t(\nu)]dtd\nu. \tag{40}$$

4) F_4—flux originating in the clear atmosphere lower down:

$$F_4=2\pi\int_0^{2500\text{ cm}^{-1}}\int_{\tau_0}^{\tau_g\text{ or }\tau_c} B_\nu[T(t)]\times\mathrm{Ei}_2[t(\nu)-\tau_0(\nu)]dtd\nu. \tag{41}$$

In these equations, $B_\nu(T)$ is the Planck emission at wavenumber ν and temperature T, and Ei_2 and Ei_3 are the second- and third-order exponential integrals.

The net flux is then obtained by subtracting the downward directed fluxes from the upward directed fluxes, i.e.,

$$F=F_2+F_4-[F_1+F_3].$$

Thus, net fluxes are computed at the 10 levels which bound the 9 layers of the dynamical model. By differencing these fluxes across the 9 layers, the net flux divergences ΔF within each layer are obtained. From the net flux divergences, longwave heating or cooling

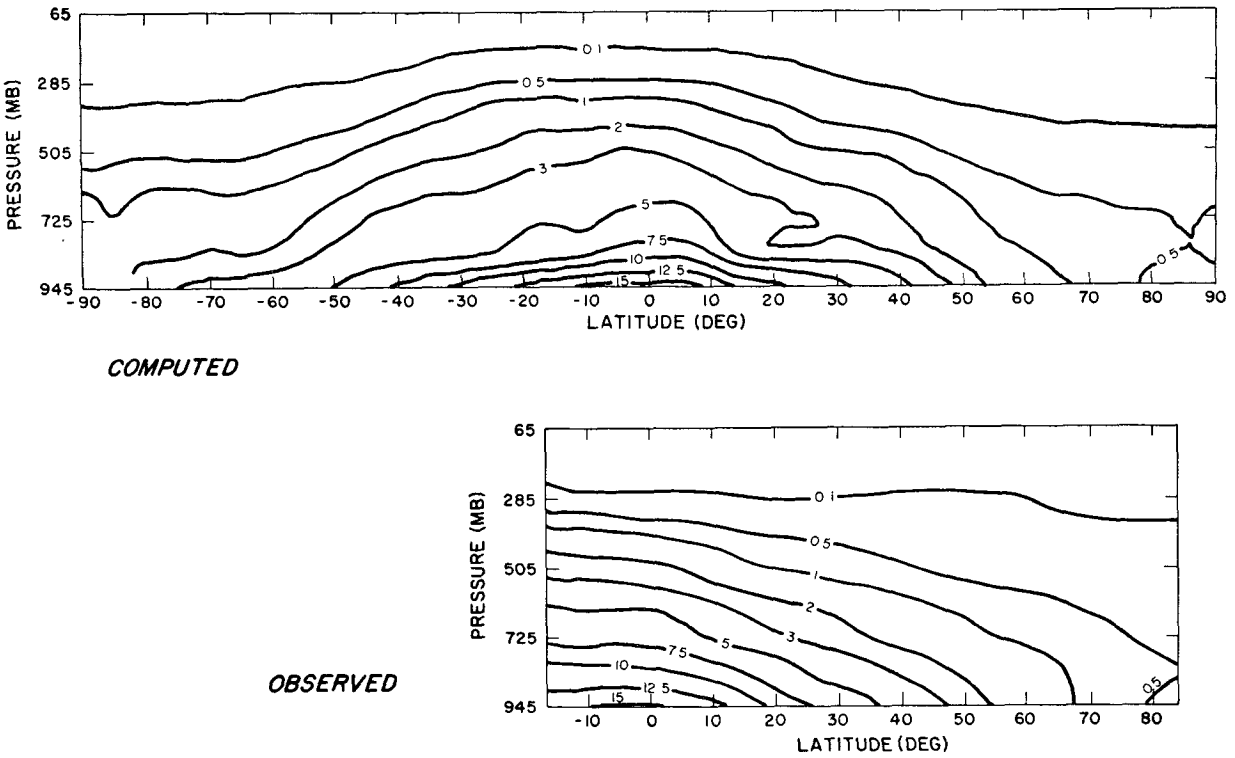

FIG. 21. Computed and observed January zonal mean fields of specific humidity (gm kg^{-1}). Observed field is based on data from Oort and Rasmusson (1971).

rates are calculated in each layer:

$$\frac{dT}{dt} = -\frac{g}{c_p}\frac{\Delta F}{\Delta p}, \tag{42}$$

where Δp is the pressure thickness of the layer and g the acceleration due to gravity.

A more complete description of the present treatment of longwave radiation, as well as a comparison with the methods used in comparable models and a discussion of results achieved with the present treatment, is in preparation (Hogan, 1974).

7. Climatology

In order to compare the model's statistics with those of the real atmosphere, a 50-day integration was carried out starting with real data for 20 December 1972. The data used for the initial condition were supplied by the National Meteorological Center (NMC) and were taken from NMC's operational data analysis north of latitude 18N and from an experimental global NMC data set south of 18N. These data did not include humidities for the model's upper three layers, so climatological values were used for these humidities. Figs. 9 and 10 show the computed time evolution of the integrated tropospheric (layers 2–9) zonal kinetic energy (K_M), eddy kinetic energy (K_E), zonal available potential energy (P_M), and eddy available potential energy (P_E) for the Northern and Southern Hemispheres. A quasi-equilibrium state was achieved within a few days, largely because of the realistic initial state. Consequently, the month of January (days 13–43, inclusive, of the integration) was selected for computing model-generated statistics. The stratosphere (layer 1) did not reach equilibrium during the 50-day integration, as illustrated in Fig. 11. Figs. 12–39 illustrate the model's statistics for January, together with graphs based on observed data, chiefly from Oort and Rasmusson's (1971) analyses of the atmosphere's mean state for January. Their data covers only latitudes 16S to 84N. Their definitions of the various statistics have been used in our analyses.

Fig. 12a shows the model's energetics for the Northern Hemisphere troposphere, calculated in the space domain. The model's energy cycle is qualitatively the same as the real atmosphere's cycle, with available zonal potential energy being converted to available eddy potential energy, and with eddy kinetic energy being drawn from available eddy potential energy and converted to zonal kinetic energy. Quantitatively, the model's energetics are consistent with the real atmosphere's annual mean energetics (Fig. 12b), the only apparent exception being zonal available potential energy. This exception is caused by seasonal variations in P_M. The observed value is an annual mean, and

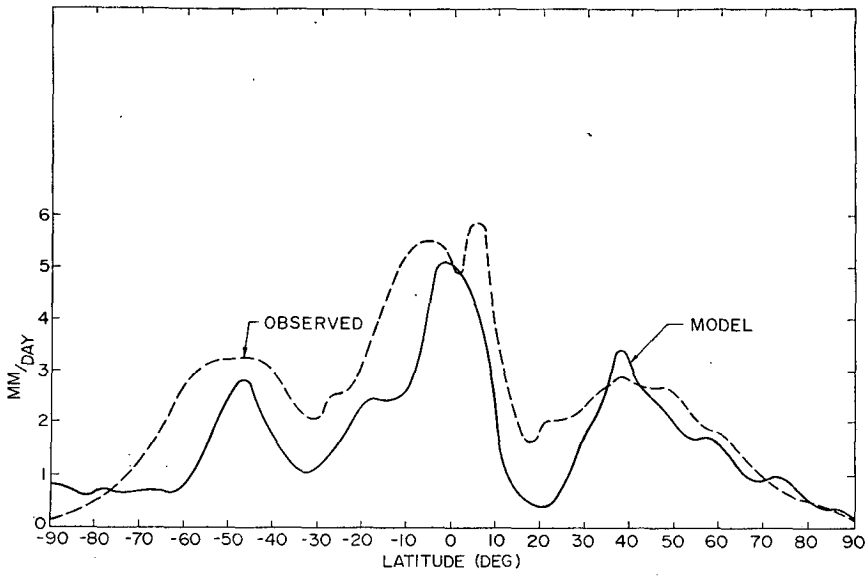

FIG. 22a. Latitudinal variation of computed January zonal mean precipitation and observed December–February zonal mean precipitation from Lvovitch and Ovtchinnikov (1964), as analyzed by Schutz and Gates (1971).

therefore not directly comparable with the model's January value. P_M was calculated from the NMC data for January 1973 and found to be 81×10^5 J m^{-2}. The model's value is in much better agreement with this value. The conversions between different forms of energy, given in Figs. 12a and 13, were computed from Oort's (1964) formulas for pressure coordinates in the space domain. These formulas are approximate, but are accurate to within a factor of 2 (Dutton and Johnson, 1967). Because of the approximations, the computed energy flows are not exactly in balance. The dissipation of energy in the interior of the model atmosphere was negligible compared to the model's surface dissipation.

Figs. 14–20 illustrate the mean wind, temperature and pressure fields. The GISS model's stratosphere (layer 1) is not in good agreement with the observations, even if one allows for its not having reached equilibrium. In designing the model, adequate stratospheric vertical resolution was sacrificed to permit improved tropospheric resolution. This was done because of the intended model applications, discussed in Section 1. The model's troposphere, however, is a

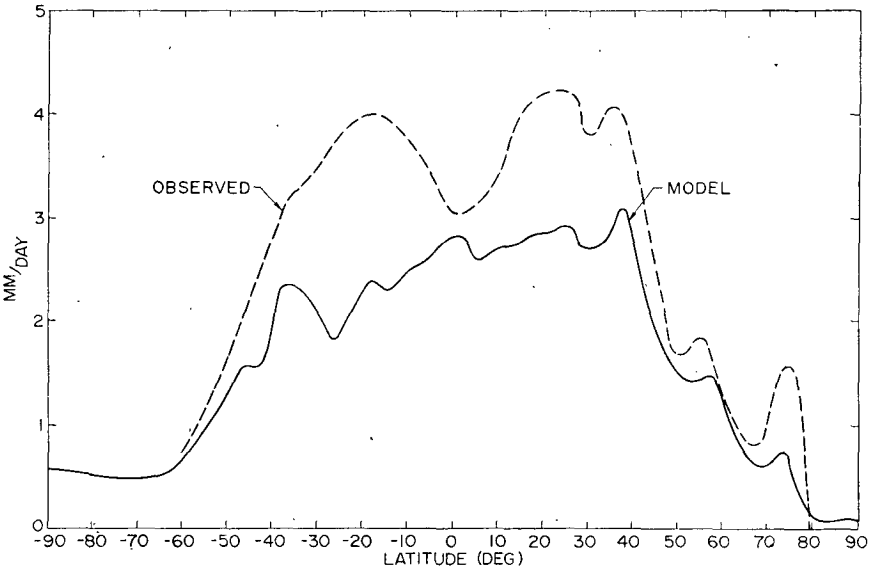

FIG. 22b. Latitudinal variation of computed January zonal mean surface evaporation and observed January zonal mean surface evaporation from Budyko (1963), as analyzed by Schutz and Gates (1971).

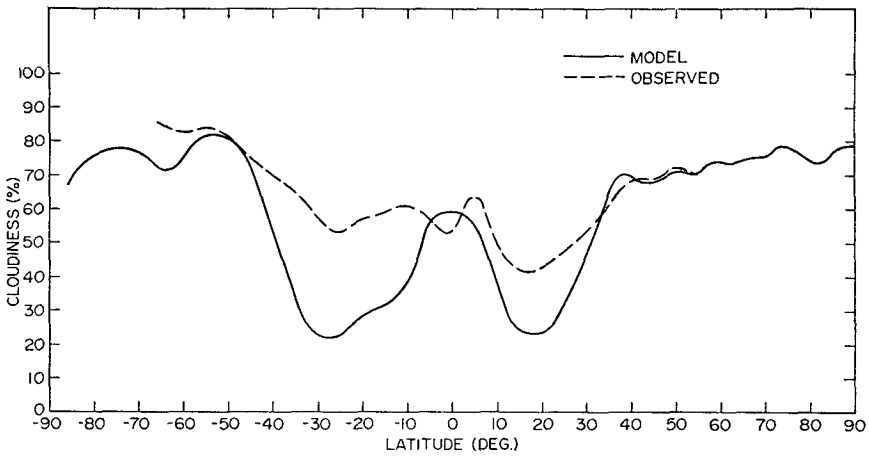

FIG. 23. Latitudinal variation of zonally averaged cloudiness from the GISS model (January mean) and from Clapp's (1964) analyses of TIROS observations (December–February).

realistic simulation of the observed troposphere. Figs. 14-17 show the normal mid-latitude westerly jet, accompanied by a Ferrel cell and strong temperature gradients; a Hadley cell in low latitudes accompanied by low-latitude easterlies; and very weak motions in polar regions with a temperature inversion during the polar night. The temperature field is statically stable everywhere (Fig. 18). Quantitatively, there are differences between the model's statistics and the normal January atmosphere. Specifically, in the Northern Hemisphere the model's westerly jet is too broad, and the meridional circulations are too weak. The north polar regions are cold, when compared to Oort and Rasmusson's (1971) data, but they are not cold when compared to Newell *et al.*'s (1969) data. The computed January mean fields of pressure (Figs. 19 and 20) show generally realistic semi-permanent features but somewhat weak gradients.

Figs. 21–23 illustrate fields associated with the hydrologic cycle. The model's distribution of specific

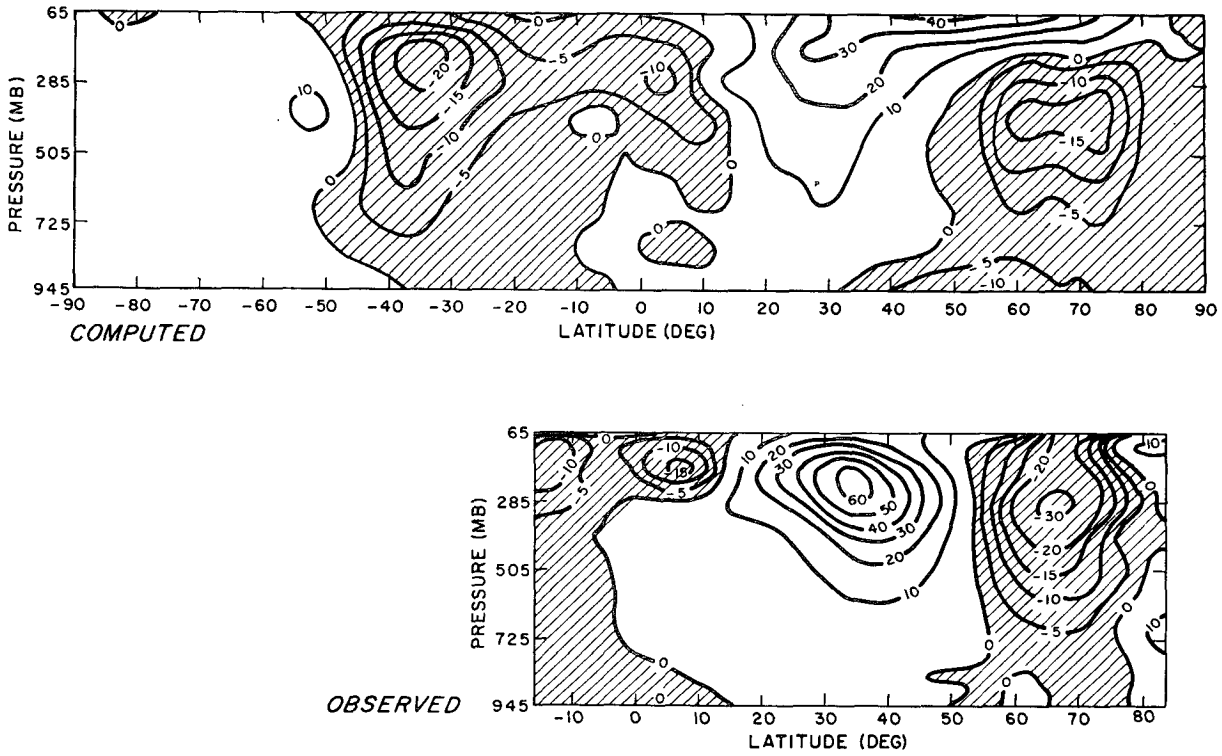

FIG. 24. Computed and observed January zonal mean fields of northward transport of westerly momentum (m^2 sec^{-2}) by eddies. Observed field is based on data from Oort and Rasmusson (1971). Negative regions are shaded.

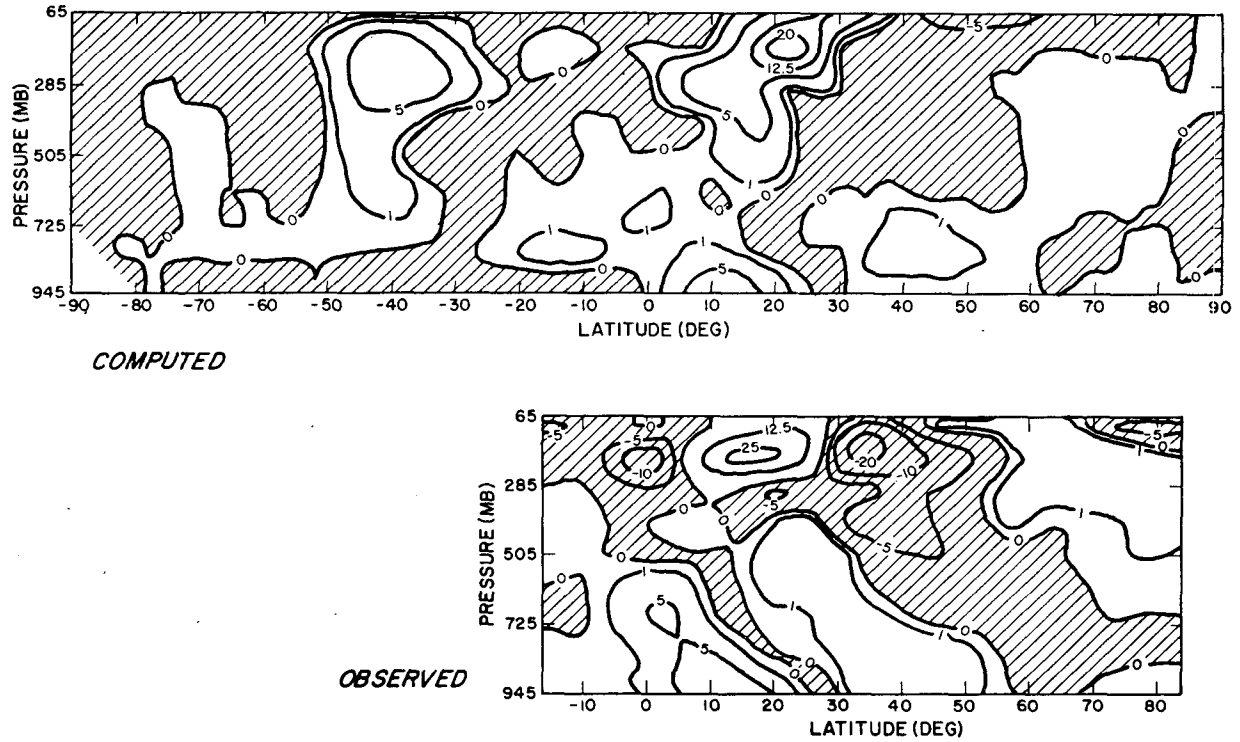

FIG. 25. As in Fig. 24 except for northward transport of westerly momentum by the mean meridional circulation.

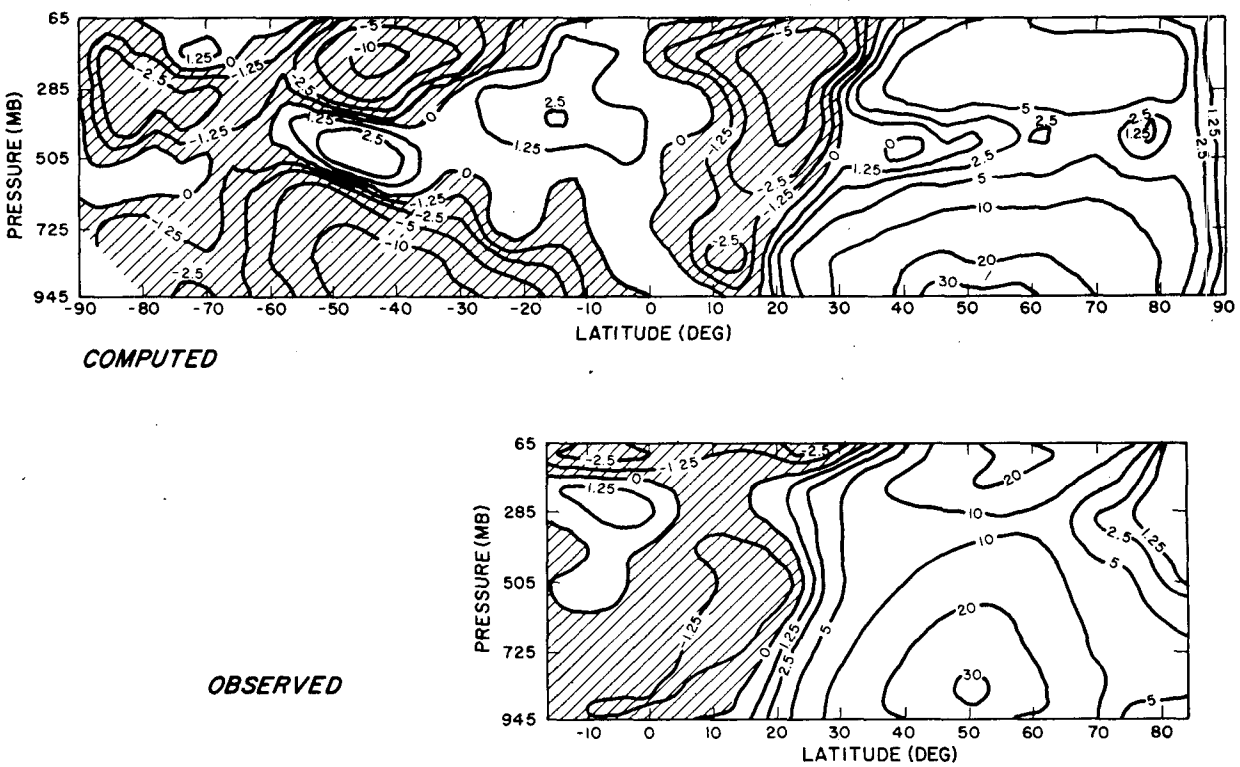

FIG. 26. As in Fig. 24 except for northward transport of sensible heat (°K m sec^{-1}) by eddies.

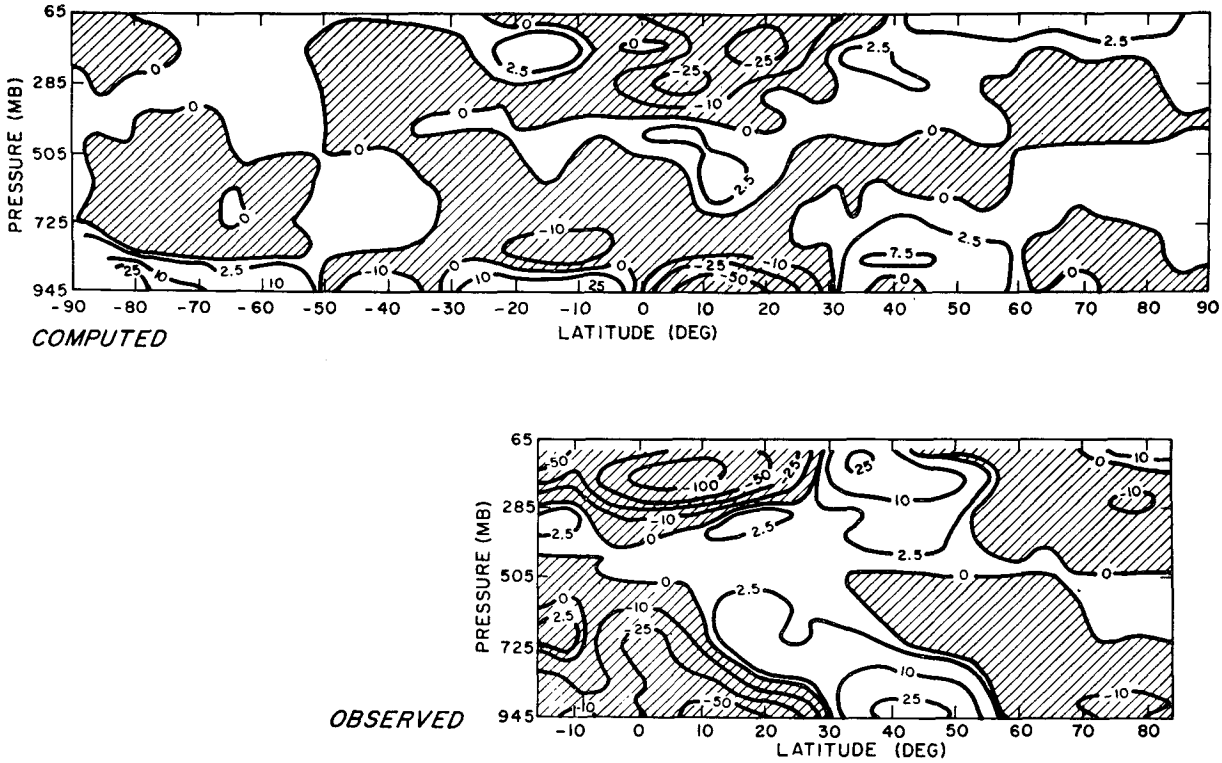

FIG. 27. As in Fig. 24 except for northward transport of sensible heat (°K m sec^{-1}) by the mean meridional circulation.

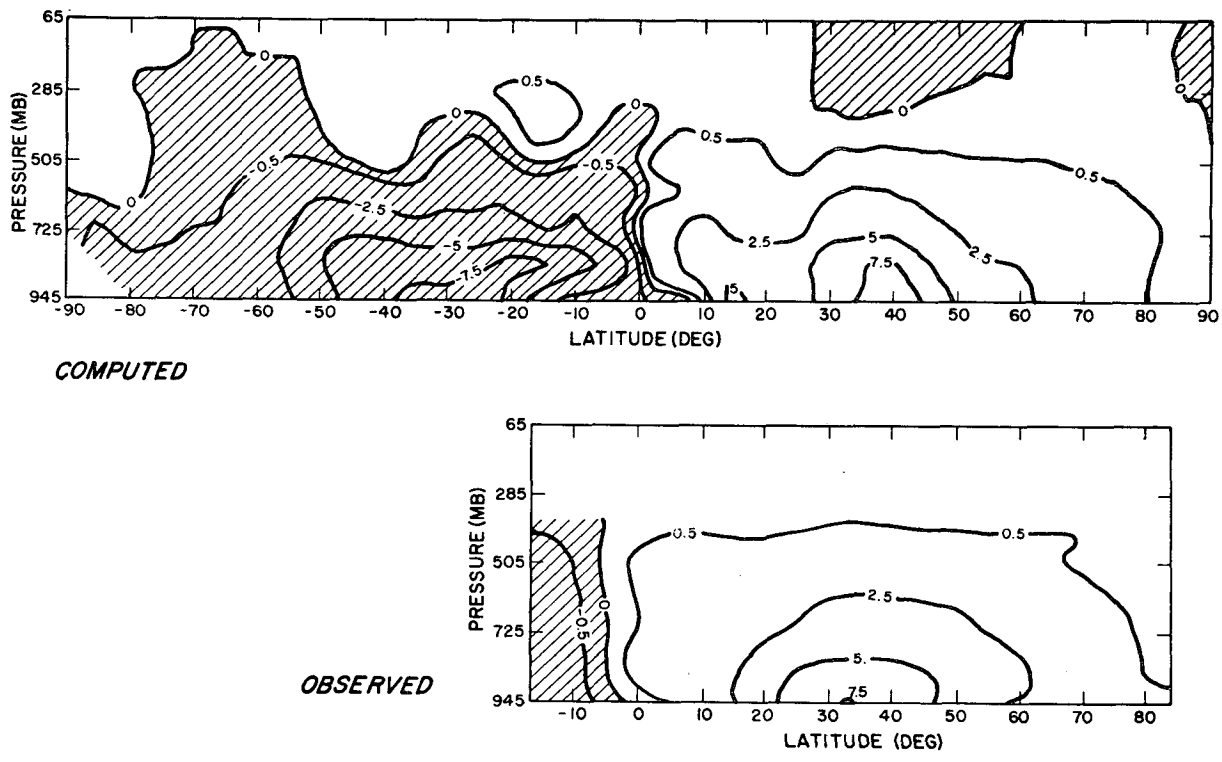

FIG. 28. As in Fig. 24 except for northward transport of water vapor [gm kg^{-1} (m sec^{-1})] by eddies.

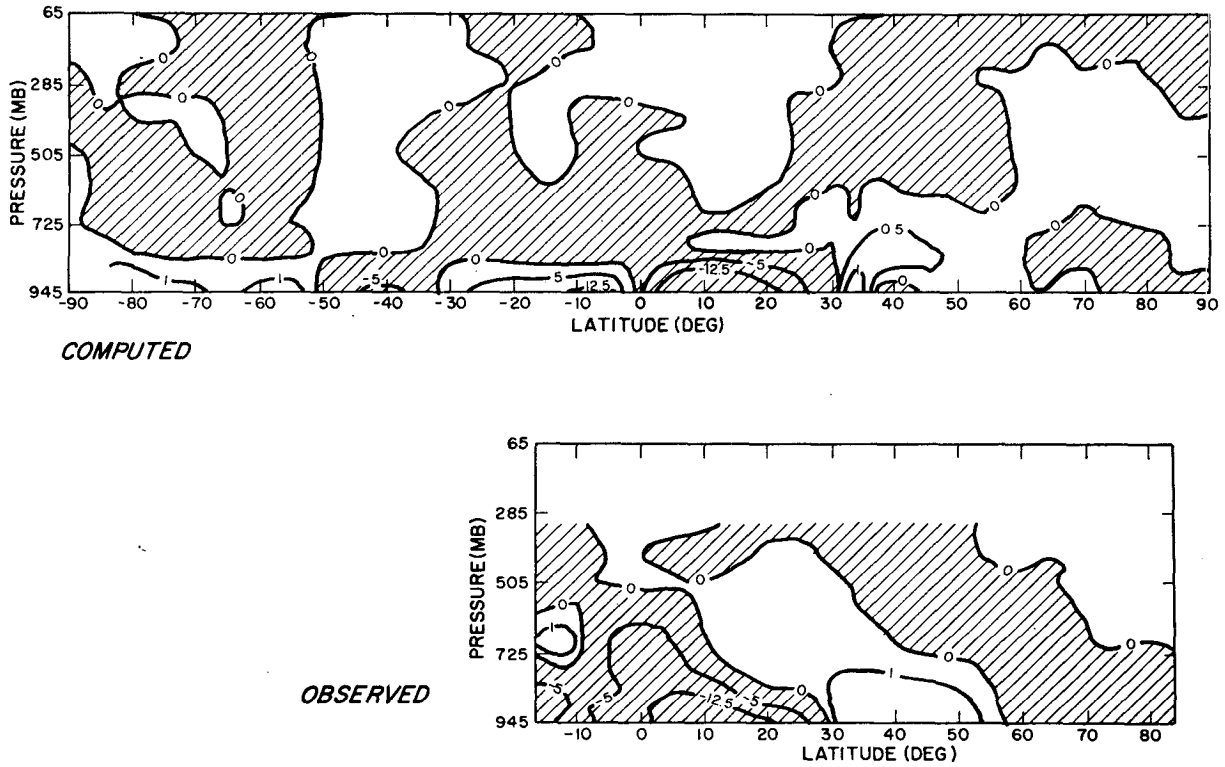

FIG. 29. As in Fig. 24 except for northward transport of water vapor [gm kg^{-1} (m sec^{-1})] by the mean meridional circulation.

humidity (Fig. 21) is quite realistic. The precipitation (Fig. 22a) has realistic maxima in low and mid-latitudes, but the minima in the subtropics are too low. The distribution of evaporation (Fig. 22b) shows the observed maximum in low latitudes, but it is underestimated. The model-generated cloudiness (Fig. 23) shows the observed minima in the subtropics, although these minima are again too low. The model's mean global cloud cover is 52%, while that of the actual atmosphere is 53% (Sasamori *et al.*, 1972). The mean global convective cloud cover is 12.5%, a realistic value (London, 1957). The computed mean global albedo is 32%, with a variability of ~2% due to changes in cloud type and location, and water vapor distribution. This value is in good agreement with recent results (31% for this season) derived from satellite observations (Vonder Haar and Suomi, 1971).

Figs. 24–33 illustrate the model's transports of momentum, sensible heat and water vapor. Conventional definitions of the transports differ from our definitions, which are taken from Oort and Rasmusson (1971). Again, the model produces a realistic simulation of the observed atmosphere: the eddy momentum transport (Fig. 24) tends to concentrate the mid-latitude jets; the eddy sensible heat transport (Fig. 26) is poleward in mid-latitudes and equatorward in low latitudes; and the eddy transports dominate in mid-latitudes while the transports by the mean meridional circulations

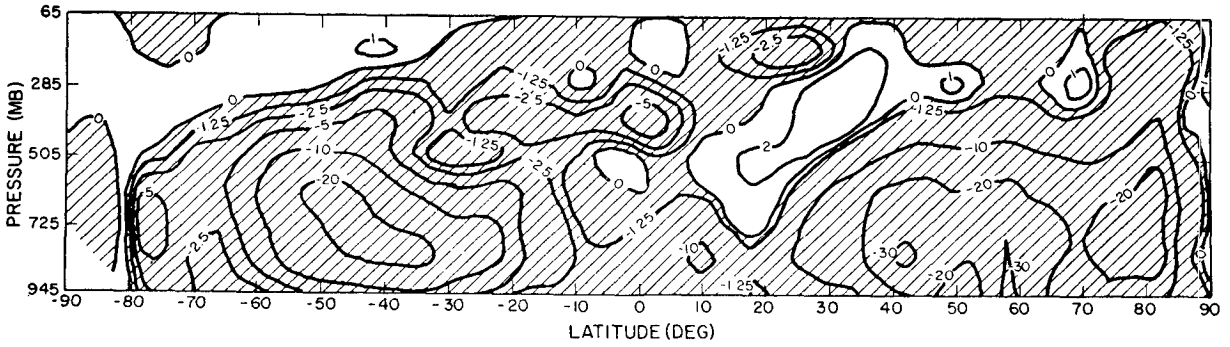

FIG. 30. Computed January zonal mean field of vertical transport of sensible heat (10^{-4} mb °K sec^{-1}) by eddies. Negative (upward) regions are shaded.

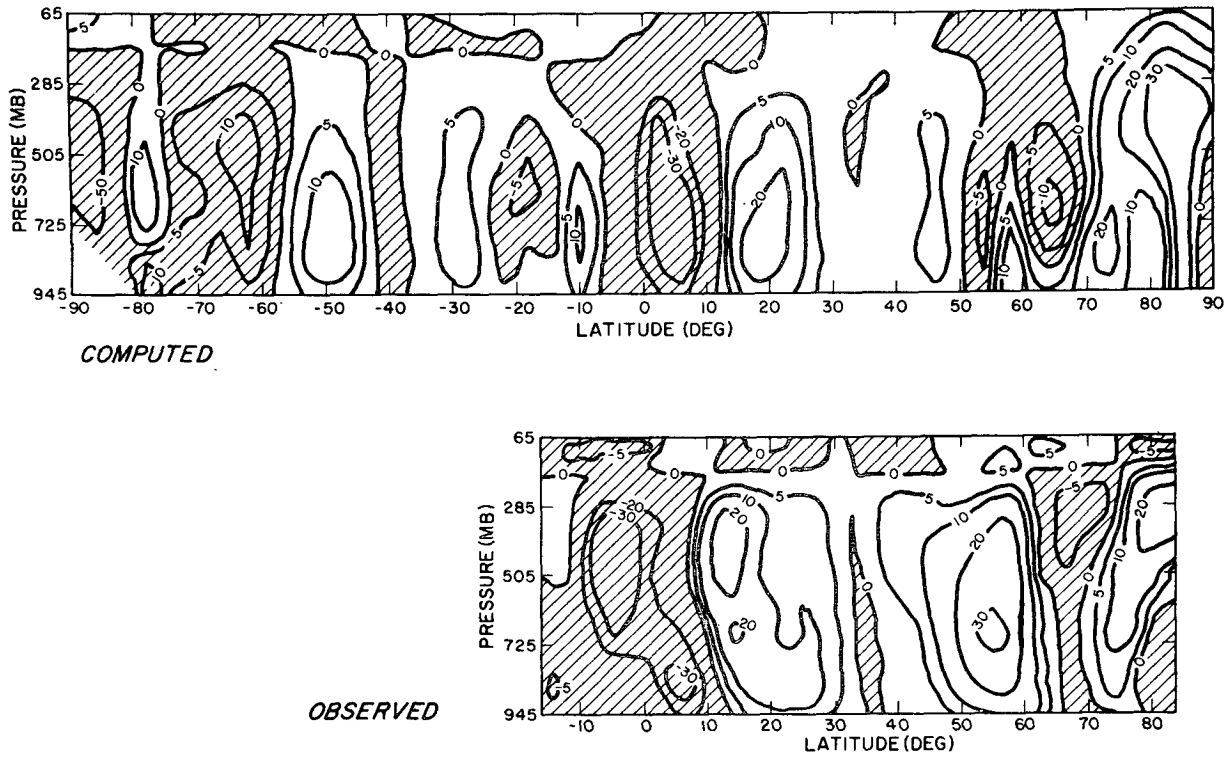

FIG. 31. Computed and observed January zonal mean fields of vertical transport of sensible heat (10^{-4} mb °K sec^{-1}) by the mean meridional circulation. Observed field is based on data from Oort and Rasmusson (1971). Negative (upward) regions are shaded.

(Figs. 25 and 27) dominate in low latitudes. Quantitatively, the transports by the mean meridional circulations in the model are systematically weaker than the mean values of these transports in the real atmosphere, in accord with the model's weaker meridional circulations noted above (Fig. 15). There are also quantitative differences between the eddy transports in the model and those observed on the average in the real atmosphere. For example, the northward eddy transport of westerly momentum (Fig. 24) in the model is about half as large as in the mean atmosphere, which is consistent with the broadness of the model's jet noted above. However, these quantitative differences in the eddy transports generally fall within the bounds of inter-annual variation (Oort and Rasmusson, 1971, Section 5E).

One good indication of the activity of the large-scale eddies in the model is the variance of the temperature field, illustrated in Fig. 34. The location and strength of the variance generated by the model's eddies agree well with those generated by the atmosphere's eddies. Another good test of the model's eddies is their kinetic energy spectrum. Fig. 35 shows the kinetic energy as a function of wavenumber in the Northern Hemisphere, defined following the conventions adopted by Saltzman (1970). The model's spectrum for wavenumbers 8–15 has approximately a -2.5 power dependence on wavenumber, rather than the

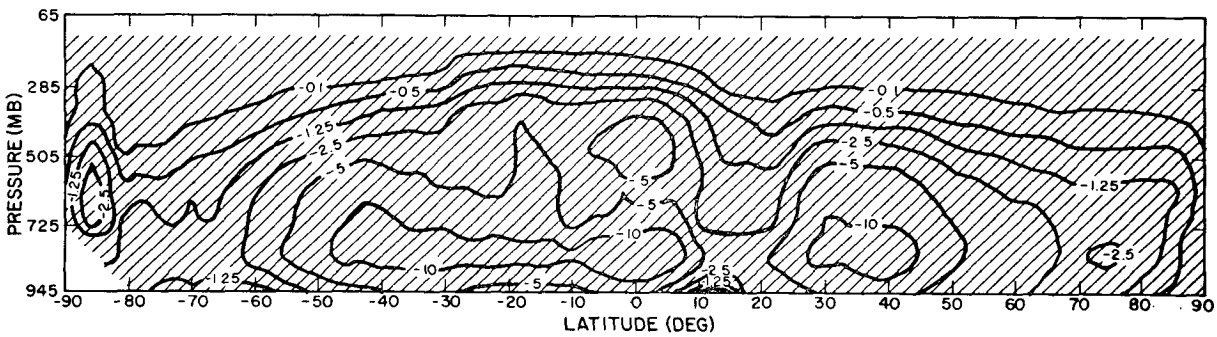

FIG. 32. As in Fig. 30 except for vertical transport of water vapor [10^{-4} mb sec^{-1} (gm kg^{-1})] by eddies.

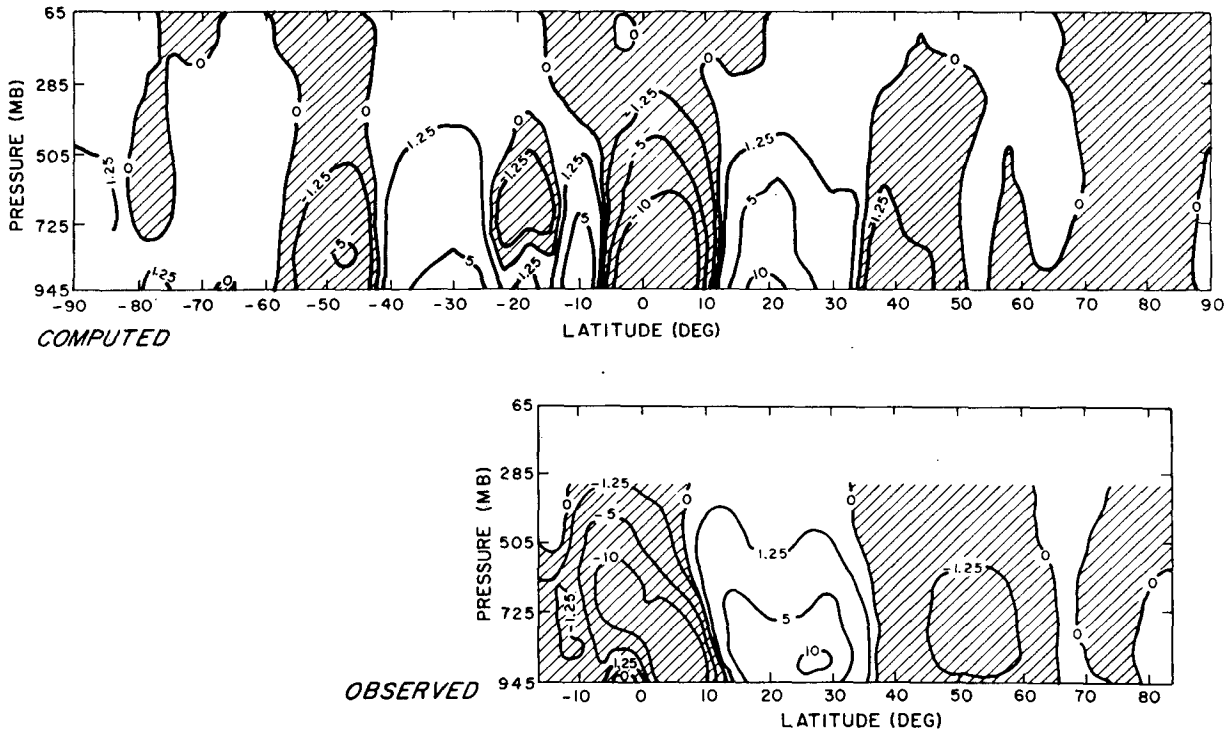

FIG. 33. As in Fig. 31 except for vertical transport of water vapor [10^{-4} mb sec^{-1} (gm kg^{-1})] by the mean meridional circulation.

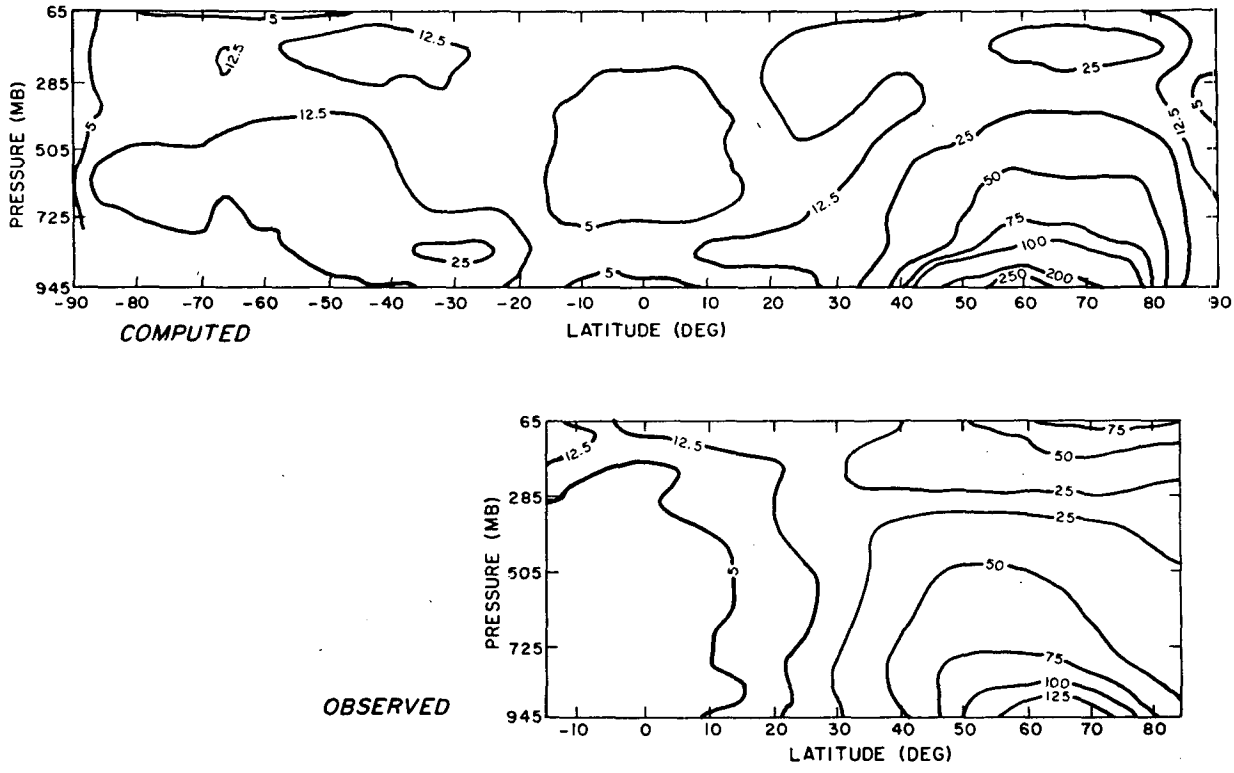

FIG. 34. Computed and observed January zonal mean fields of variance of temperature [(°K)²] due to eddies. Observed field is based on data from Oort and Rasmusson (1971).

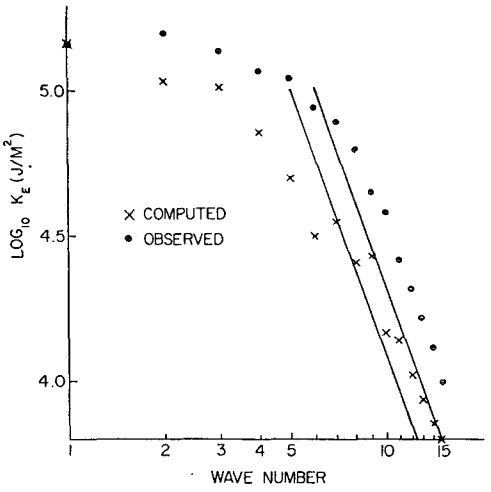

FIG. 35. Computed January mean eddy kinetic energy (K_E) vs wavenumber. The slanted lines show a -3.0 slope. The observed data of Wiin-Nielsen (1967) are also shown.

-3 power dependence of geostrophic or two-dimensional turbulence discussed by Kraichnan (1967), Leith (1968), and Charney (1971). The observed results of Wiin-Nielsen (1967) for the annual mean spectrum are also shown in Fig. 35. The model spectrum is consistently lower than Wiin-Nielsen's spectrum, which is based on data from an unusually active year. The total eddy kinetic energy in Wiin-Nielsen's spectrum is $\sim 14\times10^5$ J m^{-2}, in comparison to 7×10^5 J m^{-2} as obtained by Oort (see Fig. 12b) and 6×10^5 J m^{-2} in the model (see Fig. 12a).

Figs. 36–39 illustrate the model-generated heating rates due to radiation, condensation and convection. The model's radiative heating rates are in qualitative agreement with those of London (1957), Newell *et al.* (1969) and Dopplick (1972). They show realistic maxima in the heating by solar radiation (Fig. 36) in the mid-troposphere and stratosphere of the summer hemisphere, and a realistic maximum in the cooling by longwave radiation (Fig. 37) in low latitudes. The heating rate by supersaturation condensation (Fig. 38) shows maxima in mid- and low-latitudes, while that due to convection (Fig. 39) shows a strong maximum near the equator.

8. Short-range forecasts

To test the short-range forecasting ability of the model, five 2-day forecasts were carried out from initial states in late December 1972 and January 1973. Global initial states were constructed in the manner described in Section 7, by simply interpolating the NMC objective analysis onto the GISS model grid, with no "initialization." The forecasts were verified at 12, 24, 36 and 48 hr against the NMC analysis north of 22N. Verification statistics for these five forecasts are shown

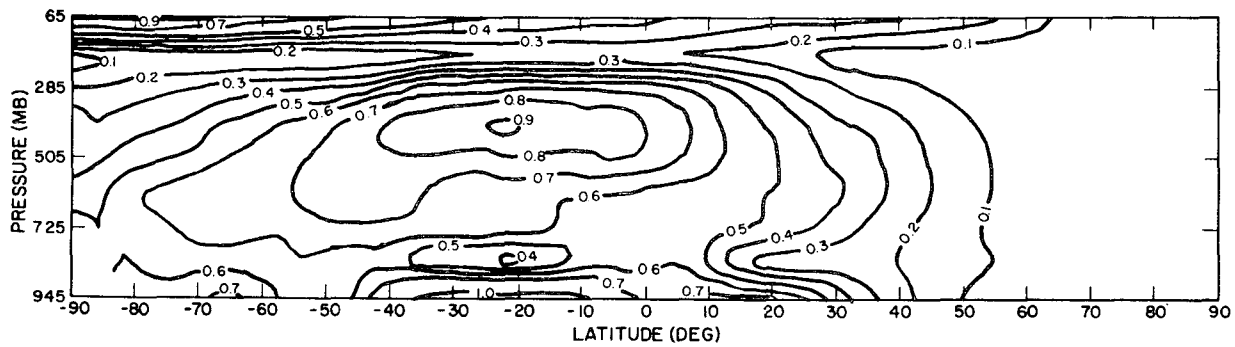

FIG. 36. Computed January zonal mean field of heating rates (°C day^{-1}) due to solar radiation.

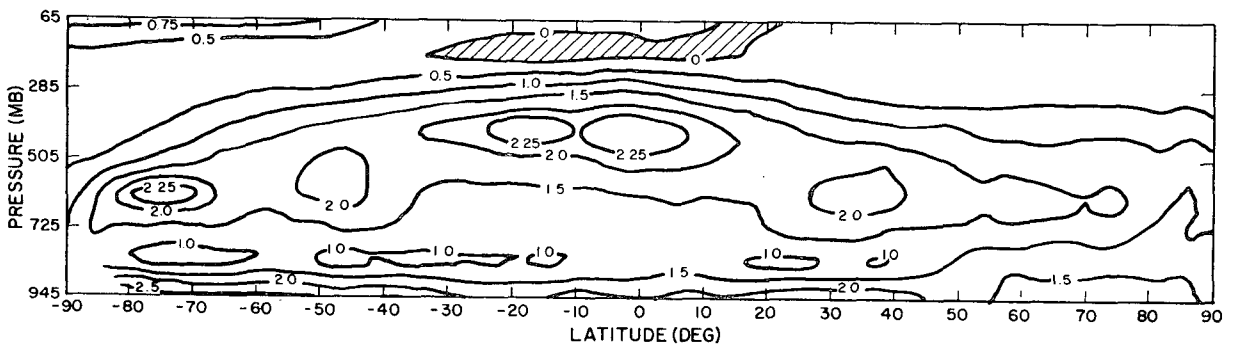

FIG. 37. Computed January zonal mean field of cooling rates (°C day^{-1}) due to terrestrial radiation. Negative regions are shaded.

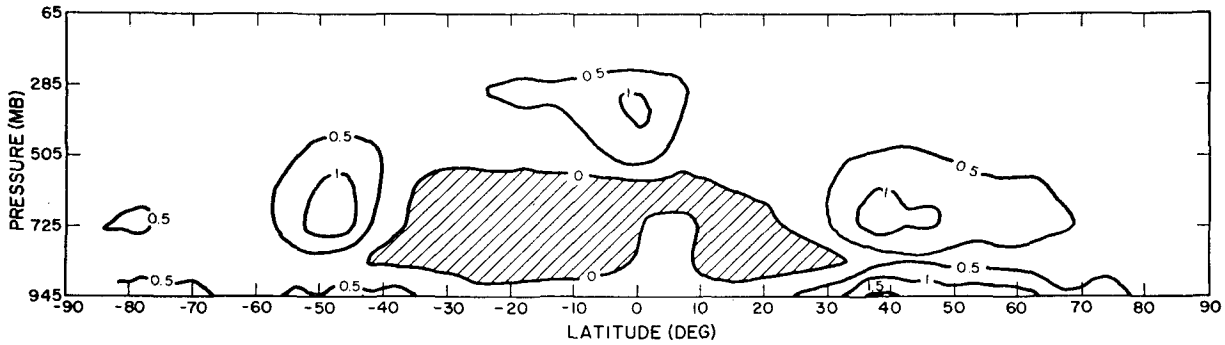

FIG. 38. Computed January zonal mean field of heating rates (°C day^{-1}) due to large-scale supersaturation. Negative regions are shaded.

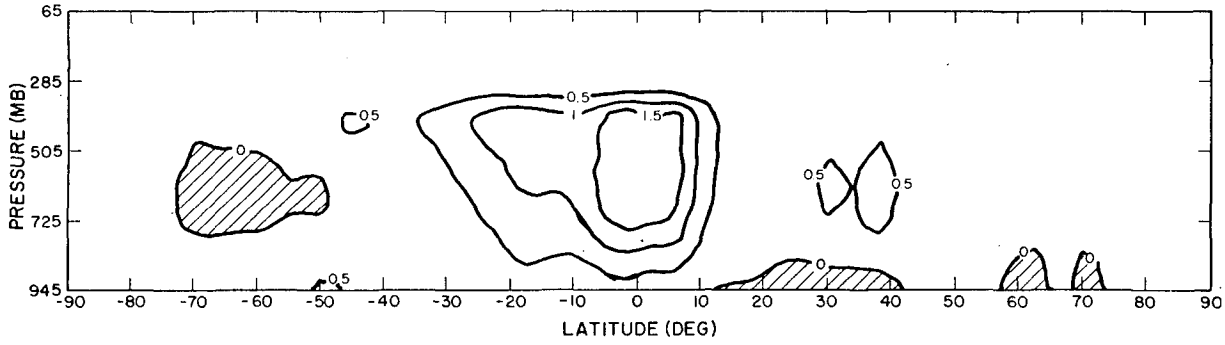

FIG. 39. Computed January zonal mean field of heating rates (°C day^{-1}) due to parameterized sub grid-scale moist convection. Negative regions are shaded.

in Table 4. Also shown for comparison are the mean January 1973 500-mb forecast height errors from NMC's operational model. These data were supplied by NMC and are cited with permission. The NMC and GISS models apparently have comparable skill in forecasting 500-mb heights. This statistic is sensitive to smoothing, however, and is not an adequate measure of overall forecasting skill. Additional verification statistics are contained in a forthcoming paper (Druyan, 1974).

To further illustrate the short-range forecasting properties of the GISS model, we have examined in some detail the first two days of the long integration described in Section 7. The sea-level pressure and 500-mb height fields were compared after 24 and 48 hr with the NMC analysis in the area north of 22N. Results in the area between the eastern Pacific and the western Atlantic are shown in the accompanying figures (40–49), and the evolution of the sea-level pressure and 500-mb height fields is described below. In Figs. 41 and 43, the sea-level pressure at each grid point has been smoothed by weighting the unsmoothed grid point value equally with the arithmetic mean of the unsmoothed values at the four surrounding grid points.

The 24-hr sea-level pressure forecast (Fig. 41) has been somewhat slow in moving a deep pressure system eastward from northern Greenland. It does show cor-

TABLE 4. Verification statistics at 12-hr intervals for 2-day forecasts. Shown are both mean values and standard deviations (in parentheses) for five forecasts. These statistics are rms differences between computed fields and NMC objective analyses north of 22N. For 500-mb heights, mean January 1973 rms differences between NMC primitive equation model forecasts and objective analyses are also shown.

Elapsed time (hr)	Sea level pressure error (mb)		Temperature error, levels 1–9 (°K)		Zonal wind error, levels 1–9 (m sec^{-1})		500-mb height error (m) GISS model		NMC forecast
12	3.7	(0.5)	2.25	(0.19)	5.25	(0.45)	32.3	(4.1)	31.8
24	4.7	(0.4)	2.88	(0.18)	6.43	(0.53)	39.7	(2.8)	39.2
36	6.0	(0.4)	3.45	(0.06)	7.53	(0.37)	54.6	(4.6)	53.4
48	7.3	(0.3)	3.86	(0.18)	8.46	(0.73)	62.3	(6.4)	65.2

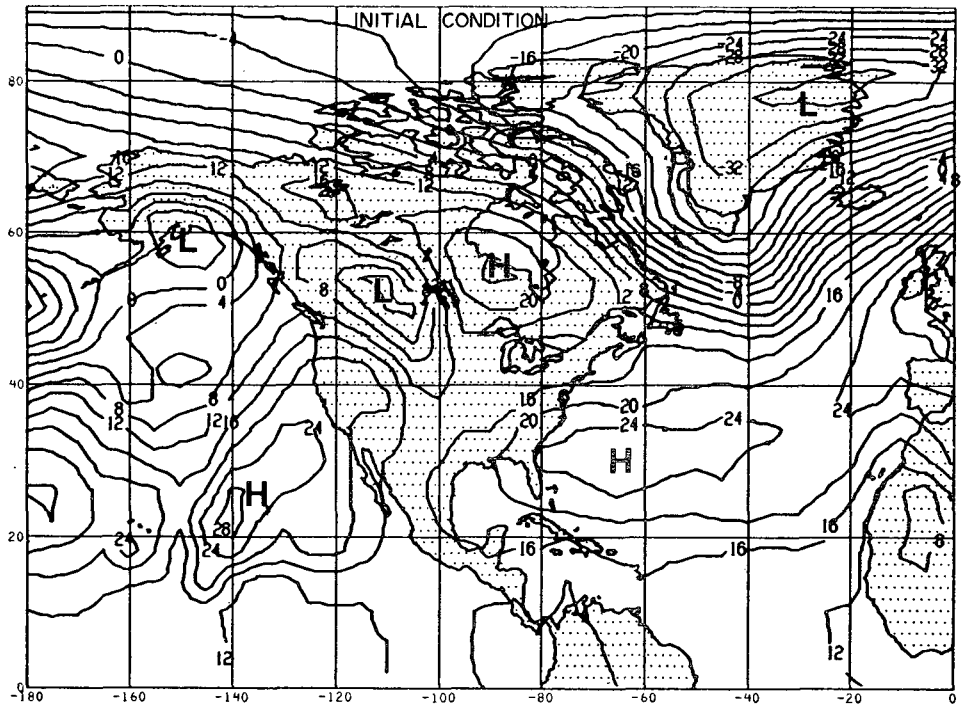

FIG. 40. Initial sea-level pressure, 0000 GMT 20 December 1972. Units: millibars −1000 for Figs. 40–44.

rectly the persistence of the strong southwest-to-northeast circulation over the northeast Atlantic, although the pressure gradient is slightly too weak. The high pressure ridge over the Atlantic is at proper strength, and the area of maximum pressure is forecast slightly to the southwest of its verified position. A high pressure system built an additional 5 mb during its 24-hr trajectory from Hudson's Bay to southern Quebec prov-

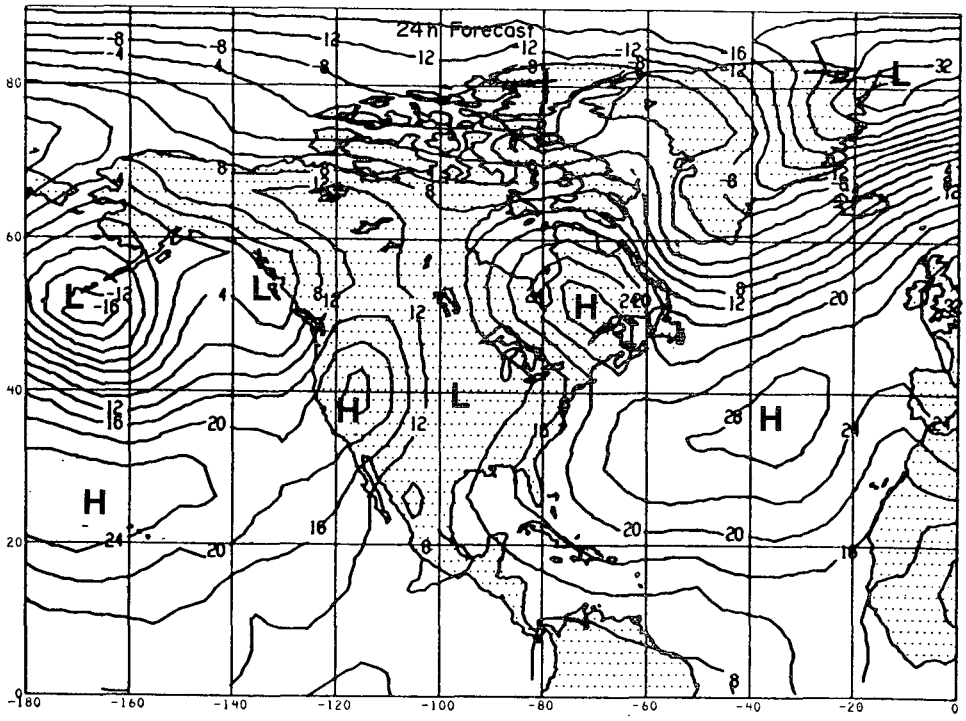

FIG. 41. Model 24-hr forecast sea-level pressure at 0000 GMT 21 December 1972.

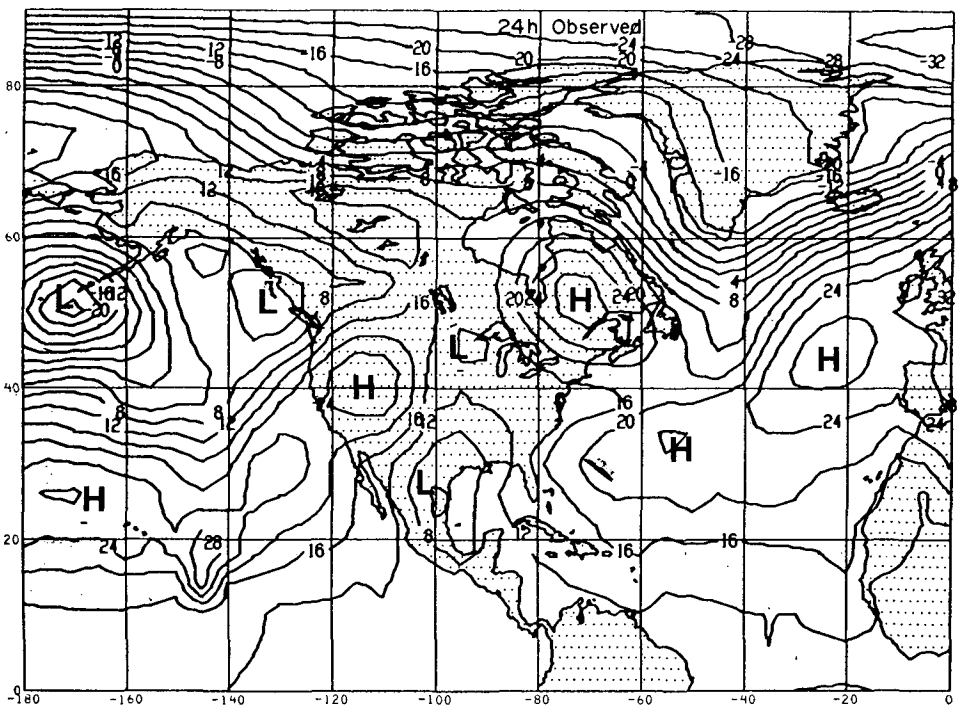

FIG. 42. Observed 24-hr sea-level pressure at 0000 GMT 21 December 1972.

ince; its evolution has been forecast very accurately. A low pressure area moved southeastward from Alberta, stretched into a trough along a Mexico-North Dakota line, and filled about 4 mb at the southern end and 12 mb at the northern; the 24-hr forecast shows a like trend. The forecast trough is well positioned, 4 mb too shallow over Mexico and only about 3 mb too low over North Dakota. High pressure has moved in from the Pacific Ocean to the western United States and the 24-hr forecast in this region is generally accurate as to

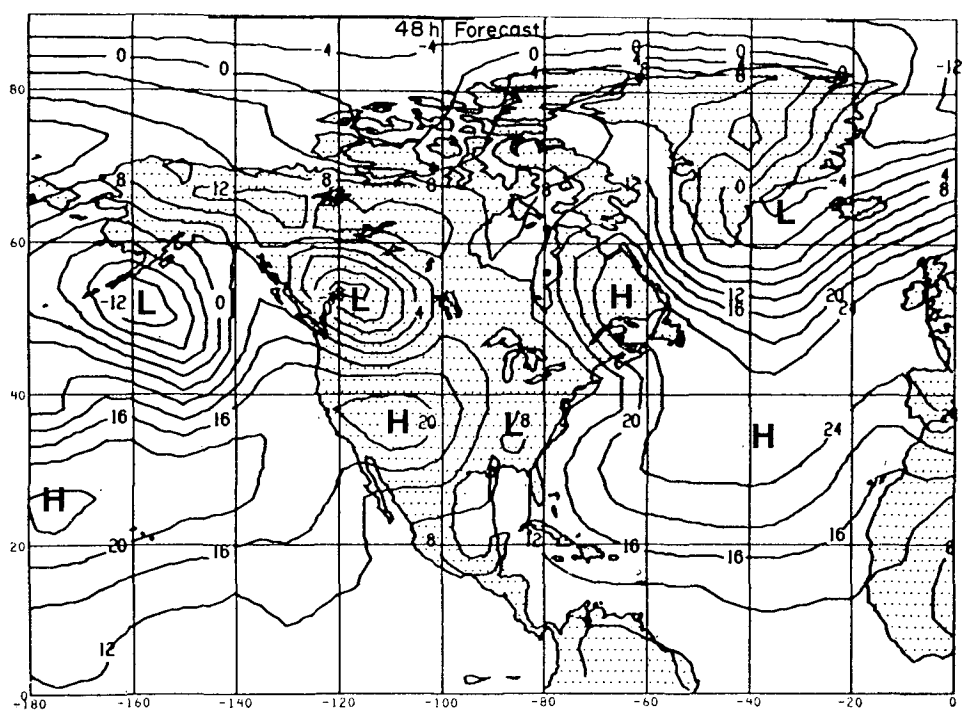

FIG. 43. Model 48-hr sea-level pressure at 0000 GMT 22 December 1972.

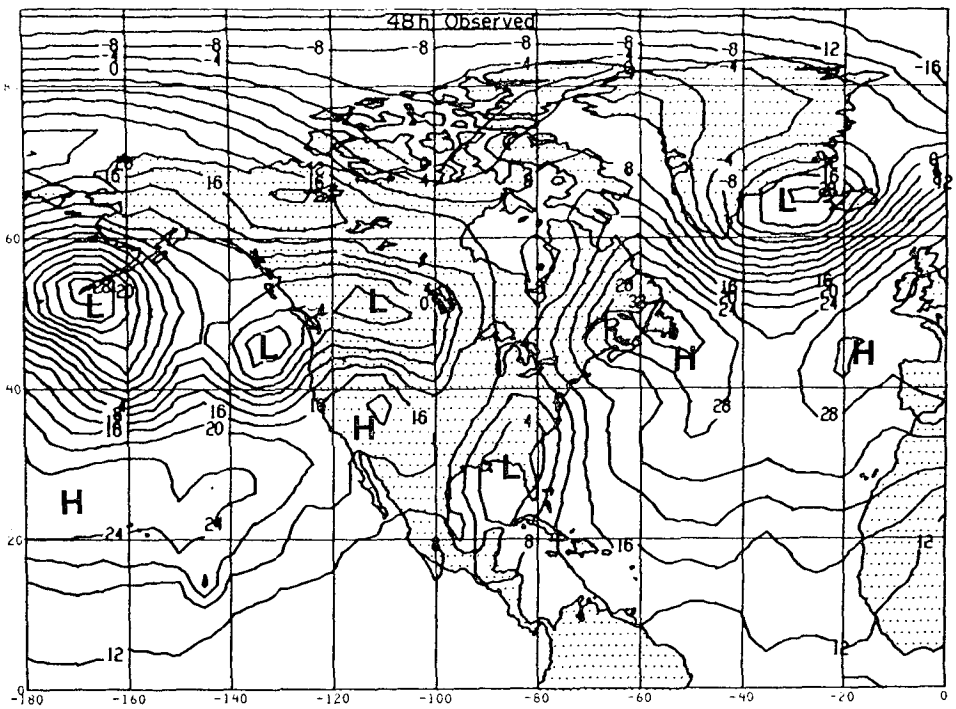

FIG. 44. Observed 48-hr sea level pressure at 0000 GMT 22 December 1972.

maximum pressure, position and pressure gradient. Both the forecast and verification charts show an 8-mb filling of the low pressure trough that has moved southeastward from southern Alaska. A deep low has moved eastward to the Aleutians and the model has forecast its position almost perfectly and its central pressure to within 3 mb.

At 48 hr after the initial condition, a new low that developed near Iceland (Fig. 44) has not been forecast, and the pressure gradient south of this region remains

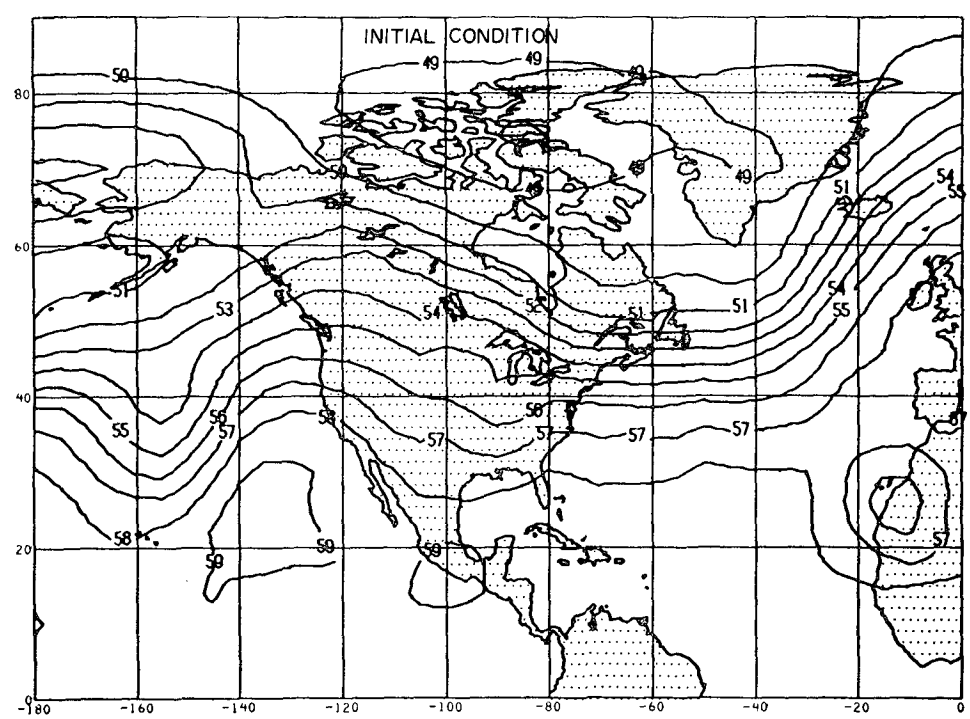

FIG. 45. Initial 500-mb heights at 0000 GMT 20 December 1972. Units: 10^2 m for Figs. 45–49.

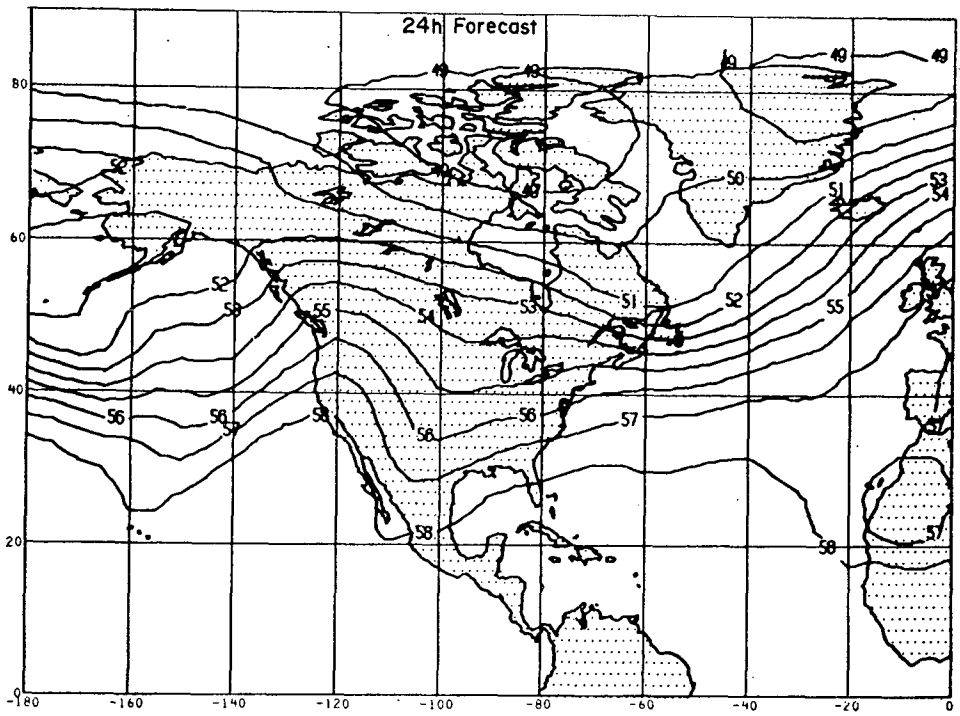

FIG. 46. Model 24-hr forecast 500-mb heights at 0000 GMT 21 December 1972.

under-forecast. The U-shaped ridge over the Atlantic Ocean is evident on the 48-hr prognosis, although the maximum pressures have not been forecast high enough. The low pressure trough has been correctly moved eastward to a Michigan/Gulf of Mexico orientation, but pressures are forecast about 6 mb too high at the southern end. High pressure forecast for the western United States is about 2 mb too shallow, and the strong west-to-east circulation over the northwestern United States has been duplicated. Rapid deepening of the low pressure area over western Canada has been forecast; the actual pressure distribution, however, shows two pressure minima, one over the continent and one southeast of Vancouver Island. The 48-hr forecast has consolidated the distribution into one deep low over British Columbia, which is slightly too intense. The stationary low over the Aleutians has deepened an additional 4 mb in the second 24-hr forecast period, whereas the forecast has allowed a 4-mb filling. The high pressure ridge that persists over much of the eastern Pacific Ocean is well depicted, with 48-hr forecast pressures only 2–4 mb too low along the ridge line.

At 24 hr after the initial conditions (Fig. 45), a weak 500-mb trough has sharpened slightly at 55W (Fig. 47). The forecast (Fig. 46) of the 500-mb heights has organized the trough axis to within a few degrees of longitude of this verified position. A second 500-mb trough has formed over the south central United States and the forecast has predicted it. Heights have not been forecast low enough over this region, however, and the ridge over the western United States is forecast slightly west of the verified position. As a result the forecast does not show the implied Canada-to-Texas trajectory of the circulation. The forecast of a short 500-mb wave over the eastern Pacific is slightly slow, causing it to lag behind its verified position at 40N, 160W. The forecast is also slow in moving an impulse further to the south.

The 48-hr forecast of the 500-mb height field (Fig. 48) resembles the observed field (Fig. 49) quite well over the Atlantic Ocean. The trough over the United States deepened and sharpened further in the second 24 hr and moved about 8° longitude toward the east. The 500-mb forecast has not deepened this trough at all, and the southern end of its axis is about 5° longitude too far to the west. The ridge over the western United States is well placed in the forecast. Errors in predicting speed of short waves over the Pacific Ocean have made any meaningful comparison there impossible. The upper-air extension of the deep Aleutian cyclone verifies at the correct minimum height value and slightly too far north.

9. Summary

We have presented two calculations designed to check the GISS model's ability to simulate the real atmosphere. The first was a 50-day integration of the GISS model, initialized with observational data for 0000 GMT 20 December 1972. We compared statistics from the 13th to the 43rd days (January) of this

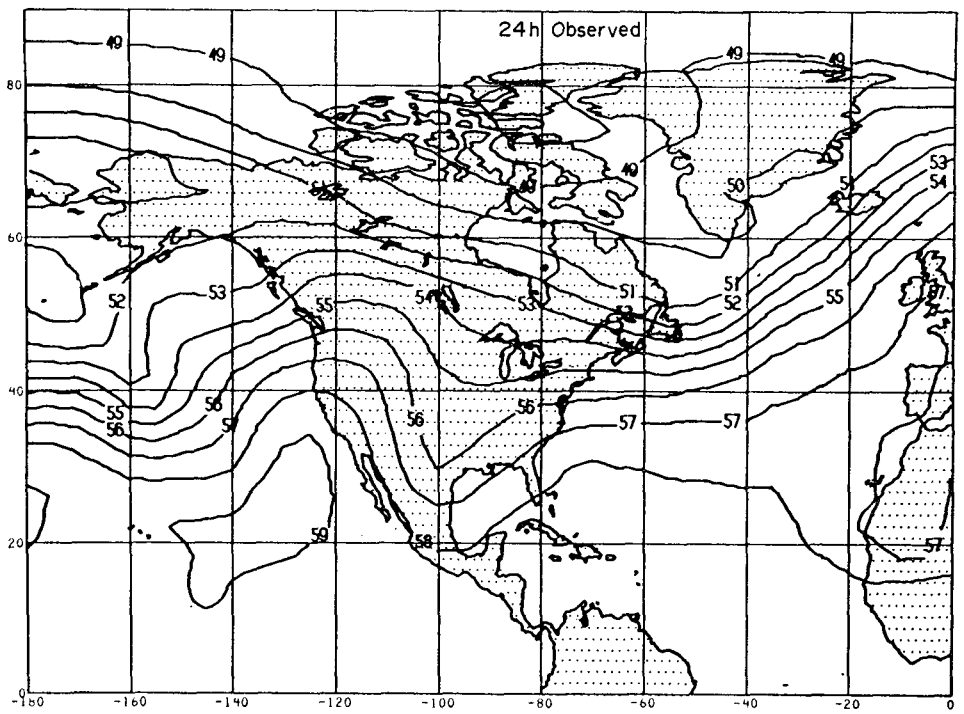

FIG. 47. Observed 24-hr 500-mb heights at 0000 GMT 21 December 1972.

integration with climatological data. During this period, the model troposphere is in near equilibrium, and its energy cycle and spectrum are realistic. The computed zonal mean fields of wind, temperature, humidity, transports, diabatic heating, evaporation, precipitation, and cloud cover generally agree well with climatological data.

The second calculation consisted of five 2-day forecasting experiments. These forecasts, verified against observational data north of 22N, yield 48-hr average

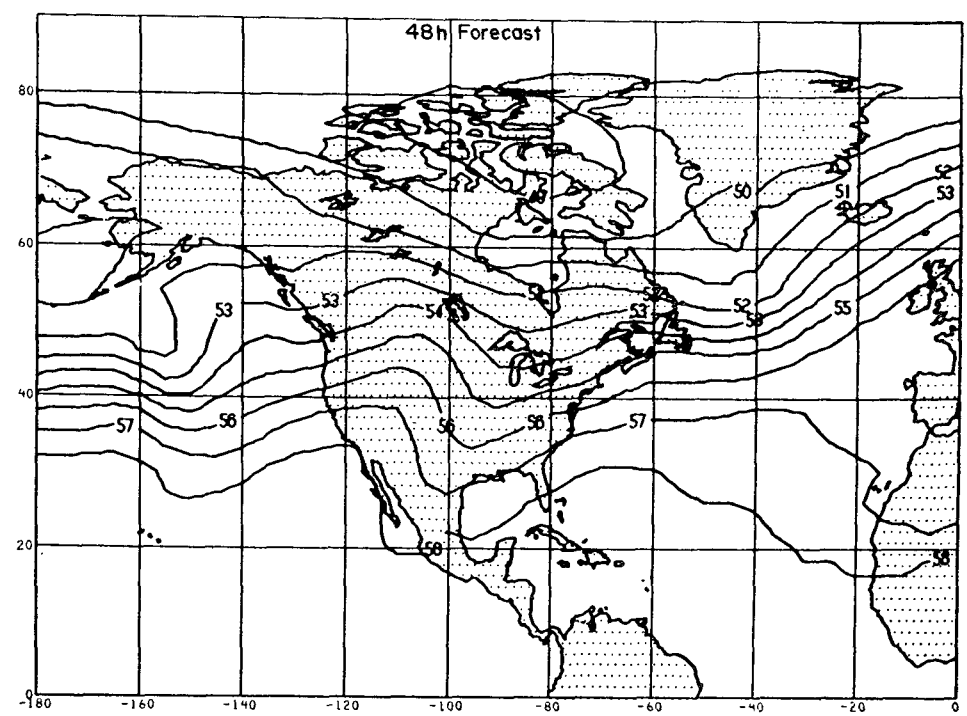

FIG. 48. Model 48-hr forecast 500-mb heights at 0000 GMT 22 December 1972.

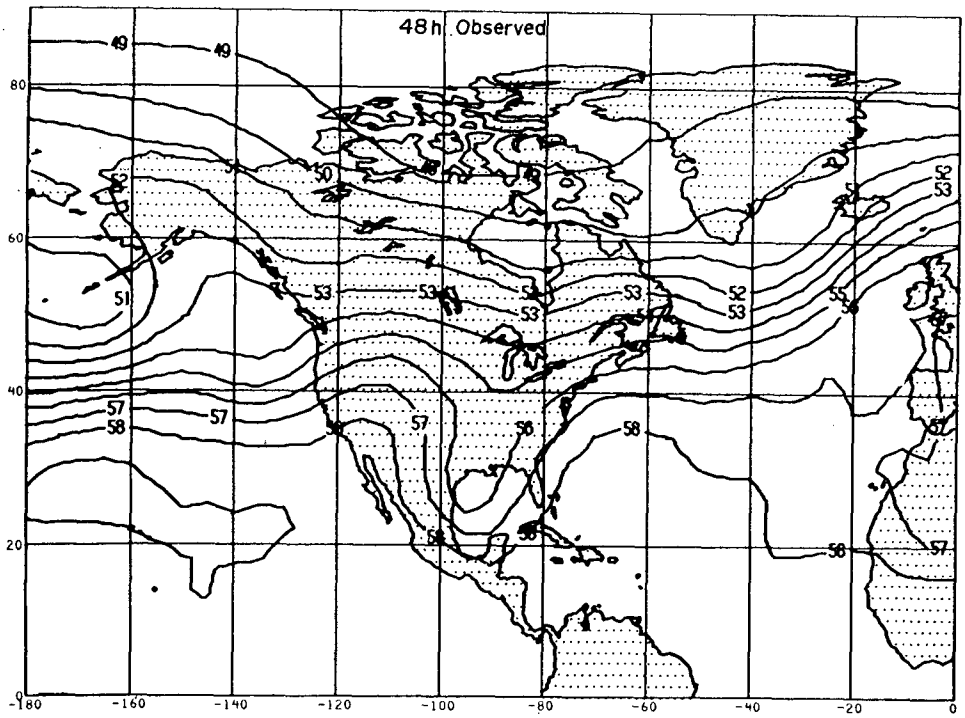

FIG. 49. Observed 48-hr 500-mb heights at 0000 GMT 22 December 1972.

rms errors of 7.2 mb for sea level pressure, 3.9K for average temperature, and 62 m for 500-mb height. The evolution of the major features of the sea level pressure and 500-mb height fields for 20 and 21 December was forecast with considerable skill.

Both of these checks were necessary since the GISS model has been designed for uses which require combining the short-range forecasting skill of the operational prediction model with the long-term stability, energetic consistency, and climatological verisimilitude of the general circulation model. In particular, it has been and will be used in observing system simulations, four-dimensional data assimilation studies, and experimental extended-range forecasting. Further tests of the model are planned, and model development will continue.

Acknowledgments. Profs. A. Arakawa and Y. Mintz of the University of California at Los Angeles have provided programs, documentation, and generous advice for several versions of their general circulation model, and we are deeply indebted to them. We are also grateful to Dr. A. Oort of the NOAA Geophysical Fluid Dynamics Laboratory at Princeton, who supplied us with copies of his observational analyses and patiently answered many questions about them. W. J. Quirk has been supported by a National Research Council–National Aeronautics and Space Administration Postdoctoral Research Associateship.

REFERENCES

Arakawa, A. 1966: Computational design for long-term numerical integration of the equations of fluid motion: Two dimensional incompressible flow. Part I. *J. Comput. Phys.*, **1**, 119–143.

——, 1970: Numerical simulation of large-scale atmospheric motions. *Numerical Solution of Field Problems in Continuum Physics*, Providence, R. I., Amer. Math. Soc., 24–40.

——, 1972: Design of the UCLA atmospheric general circulation model. Tech. Rept. No. 7, Dept. of Meteorology, University of California at Los Angeles.

——, A. Katayama and Y. Mintz, 1969: Numerical simulation of the general circulation of the atmosphere. *Proc. WMO/IUGG Symp. Numerical Weather Prediction*, Tokyo, Japan Meteor. Agency, IV, 7, 8–12.

Benedict, W. S., and L. D. Kaplan, 1959: Calculation of line widths in H_2O–N_2 collisions. *J. Chem. Phys.*, **30**, 388–399.

Budyko, M. I., 1963: *Atlas of the Heat Balance of the Earth.* Moscow, Gidrometeorizdat, 69 pp.

Champion, D., W. O'Sullivan and S. Teweles, Eds., 1962: *United States Standard Atmosphere.* Washington, D. C., Govt. Printing Office, 278 pp.

Charney, J. G., 1971: Geostrophic turbulence. *J. Atmos. Sci.*, **28**, 1087–1095.

Clapp, P. F., 1964: Global cloud cover for seasons using TIROS nephanalyses. *Mon. Wea. Rev.*, **92**, 495–507.

Deardorff, J. W., 1967: Empirical dependence of the eddy coefficient for heat upon stability above the lowest 50 m. *J. Appl. Meteor.*, **6**, 631–643.

Dopplick, T. G., 1972: Radiative heating of the global atmosphere. *J. Atmos. Sci.*, **29**, 1278–1294.

Drayson, R., and C. Young, 1967: The frequencies and intensities of carbon dioxide absorption lines between 12 and 18 microns. Rept. No. 08183-1-1, High Altitude Engineering Lab., University of Michigan.

Druyan, L. M., 1974: Short-range forecasts with the GISS model of the global atmosphere. *Mon. Wea. Rev.* (in press).

Dutton, J. A., and D. R. Johnson, 1967: The theory of available potential energy and a variational approach to atmospheric energetics. *Advances in Geophysics*, Vol. 12, New York, Academic Press, 333–436.

Gates, W. L., 1972: The January global climate simulated by the two-level Mintz-Arakawa model: A comparison with observation. Rept. R-1005-ARPA, Rand Corporation.

——, E. S. Batten, A. B. Kahle and A. B. Nelson, 1971: A documentation of the Mintz-Arakawa two-level atmospheric general circulation model. Rept. R-877-ARPA, Rand Corporation.

Green, A. E. S., 1964: Attenuation by ozone and the earth's albedo in the middle ultraviolet. *Appl. Opt.*, **3**, 203–208.

Haltiner, G. J., 1971: *Numerical Weather Prediction*. New York, Wiley, 317 pp.

Hogan, J. S., 1974: Parameterization of terrestrial radiation for the GISS model of the global atmosphere. (In preparation.)

Holloway, J. L., Jr., and S. Manabe, 1971: Simulation of climate by a global general circulation model: I. Hydrologic cycle and heat balance. *Mon. Wea. Rev.*, **99**, 335–370.

Howard, J. N., D. E. Burch and D. Williams, 1956: Infrared transmission of synthetic atmospheres, Parts I–V. *J. Opt. Soc. Amer.*, **46**, 186–190, 237–241, 242–245, 334–338, 452–455.

Jastrow, R., and M. Halem, 1973: Simulation studies and the design of the First GARP Global Experiment. *Bull. Amer. Meteor. Soc.*, **54**, 13–21.

Joseph, J. H., 1971: On the calculation of solar radiation fluxes in the troposphere. *Solar Energy*, **13**, 251–261.

Kasahara, A., and W. Washington, 1971: General circulation experiments with a six-layer NCAR model, including orography, cloudiness and surface temperature calculations. *J. Atmos. Sci.*, **28**, 657–701.

Kraichnan, R. H. 1967: Inertial ranges in two-dimensional turbulence. *Phys. Fluids*, **10**, 1417–1423.

Labs, D., and H. Neckel, 1968: The radiation of the solar photosphere from 2000 Å to 100 μ. *Z. Astrophys.*, **69**, 1–73.

Lacis, A. A., and J. E. Hansen, 1974: A parameterization for the absorption of solar radiation in the earth's atmosphere. *J. Atmos. Sci.*, **31**, 118–133.

Leith, C. E., 1968: Diffusion approximation for two-dimensional turbulence. *Phys. Fluids*, **11**, 671–673.

London, J., 1957: A study of the atmospheric heat balance. Final Report, Contract AF19(122)—165, Dept. of Meteorology and Oceanography, New York University.

Lvovitch, M. I., and S. P. Ovtchinnikov, 1964: *Physical Geographic Atlas of the World*. Moscow, Academy of Sciences.

Manabe, S., and F. Möller, 1961: On the radiative equilibrium and heat balance of the atmosphere. *Mon. Wea. Rev.*, **89**, 503–532.

——, J. Smagorinsky and R. F. Strickler, 1965: Simulated climatology of a general circulation model with a hydrologic cycle. *Mon. Wea. Rev.*, **93**, 769–798.

——, and R. F. Strickler, 1964: Thermal equilibrium of the atmosphere with a convective adjustment. *J. Atmos. Sci.*, **21**, 361–385.

Mintz, Y., 1968: Very long-term global integration of the primitive equations of atmospheric motion: An experiment in climate simulation. *Meteor. Monogr.*, **8**, No. 30, 20–36.

Newell, R. E., D. G. Vincent, T. G. Dopplick, D. Ferraga and J. W. Kidson, 1969: The energy balance of the global atmosphere. *The Global Circulation of the Atmosphere*, G. A. Corby, Ed., London, Roy. Meteor. Soc., 42–90.

Oort, A. H., 1964: On estimates of the atmospheric energy cycle. *Mon. Wea. Rev.*, **92**, 483–493.

——, and E. R. Rasmusson, 1971: Atmospheric circulation statistics. NOAA Prof. Paper 5.

Rodgers, C. D., 1967: The radiative heat budget of the troposphere and lower stratosphere. Rept. A2, Dept. of Meteorology, Massachusetts Institute of Technology, 99 pp.

Saltzman, B., 1970: Large scale atmospheric energetics in the wavenumber domain. *Rev. Geophys. Space Phys.*, **8**, 289–302.

Sasamori, T., J. London and D. V. Hoyt, 1972: Radiation budget of the Southern Hemisphere. *Meteor. Monogr.*, **13**, No. 35, 9–23.

Schutz, C., and W. L. Gates, 1971: Global climatic data for surface, 800 mb, 400 mb: January. Rept. R-915-ARPA, Rand Corporation.

Vonder Haar, T. H., and V. E. Suomi, 1971: Measurements of the earth's radiation budget from satellites during a five-year period. Part I: Extended time and space means. *J. Atmos. Sci.*, **28**, 305–314.

Washington, W. M., and A. Kasahara, 1970: A January simulation experiment with the two-layer version of the NCAR global circulation model. *Mon. Wea. Rev.*, **98**, 559–580.

——, and L. G. Thiel, 1970: Digitized monthly mean ocean temperatures over the globe. Tech. Note 54, National Center for Atmospheric Research, 30 pp.

Wiin-Nielsen, A., 1967: On the annual variation and spectral distribution of atmospheric energy. *Tellus*, **19**, 540–559.

Yamamoto, G., 1962: Direct absorption of solar radiation by atmospheric water vapor, carbon dioxide and molecular oxygen. *J. Atmos. Sci.*, **19**, 182–188.